


# 國立交通大學

分子醫學與生物工程研究所

碩士論文

超順磁性氧化鐵奈米粒子鍵結 8G7 之磁振造影研究

The logo of National Central University (NCU) is a circular emblem. It features a gear-like outer border. Inside the circle, there is a stylized building with the letters 'E', 'S', and 'A' on its facade. Below the building, the year '1896' is inscribed. The entire logo is rendered in a light blue, semi-transparent watermark style.

8G7 mAb Conjugated SPIO Nanoparticle as Targeted MRI  
Contrast Agent for Early Diagnosis of  
Pancreatic Cancer

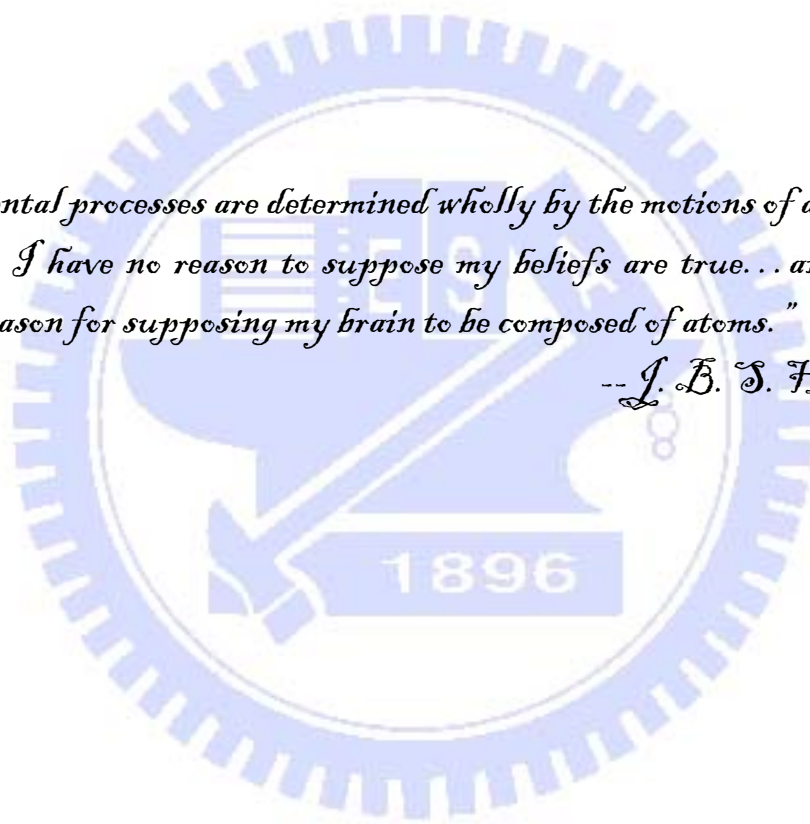
研究生：辛加安

指導教授：王雲銘 教授

中華民國九十八年十一月

*"If my mental processes are determined wholly by the motions of atoms in my brain, I have no reason to suppose my beliefs are true... and hence I have no reason for supposing my brain to be composed of atoms."*

*-- J. B. S. Hald*



# 超順磁性氧化鐵奈米粒子鍵結 8G7 之磁振造影研究

研究生: 辛加安

指導教授: 王雲銘 博士

國立交通大學分子醫學與生物工程研究所 碩士班

## 摘要

本論文的主要目的為發展高靈敏度的 MRI 對比劑以應用於胰腺癌的早期診斷。我們結合奈米技術與生物技術以設計  $T_2$  weighted MRI 對比劑。在超順磁性氧化鐵奈米粒子 ( SPIO ) 的表面修飾 mPEG -NH<sub>2</sub> , 其游離端可與 8G7 mAb 鍵合, 而這抗體對 MUC4 具有高專一性的特質。MUC4 會有異常表現於胰腺癌, 而正常胰腺與慢性胰腺炎則無。利用動態光散射儀 ( DLS ) 檢測 SPIO-mPEG-NH<sub>2</sub> 和 SPIO-mPEG-8G7 奈米粒子的流體力學的平均粒徑分佈, 分別為 37.7 和 45.9nm。SPIO-mPEG-8G7 在  $37.0 \pm 0.1$  °C 和 20 MHz 測到的 relaxivity 值,  $r_1$  和  $r_2$  , 是 24.97 和  $206.01 \text{ mM}^{-1}\text{s}^{-1}$ 。由於 SPIO-mPEG-8G7 奈米粒子的標靶能力已藉由 *in vitro* MRI 證實, 因此在有表現 MUC4 的細胞株, SPIO-mPEG - 8G7 奈米粒子可表現出顯著的磁共振對比。此外, 利用 MPCVD 合成之石墨奈米薄片 ( GNSs ) 具高產率。其結構用掃描電子顯微鏡, 透射電子顯微鏡, 選擇區域電子衍射, X 光衍射和拉曼光譜於做結構的分析。而目前以利用純碳作為  $T_2$  MRI 對比劑的實驗還在持續進行中。

# 8G7 mAb Conjugated SPIO Nanoparticle as Targeted MRI Contrast Agent for Early Diagnosis of Pancreatic Cancer

Student: Gyan Singh

Advisor: Dr. Yun-Ming Wang

Institute of Molecular Medicine and Bioengineering

National Chiao Tung University

## Abstract

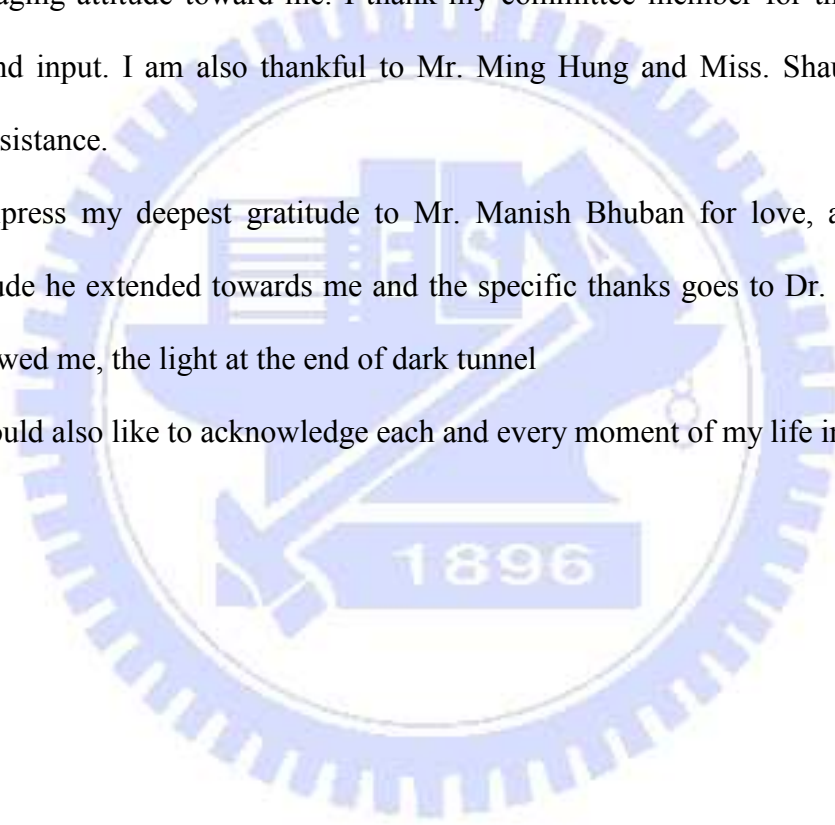
The primary objective of this thesis is to develop highly sensitive MRI contrast agent for early diagnosis of pancreatic cancer. We have exploited the novel aspects of nanotechnology and biotechnology to design  $T_2$  weighted MRI contrast agent. The superparamagnetic iron oxide nanoparticles (SPIONs) surface modified with mPEG-NH<sub>2</sub> free terminal has been conjugated with 8G7 mAb, which is highly specific to MUC4. MUC4 is abruptly expressed in pancreatic cancer with no detectable expression in normal pancreas or chronic pancreatitis. The average hydrodynamic size distribution of SPIO-mPEG-NH<sub>2</sub> and SPIO-mPEG-8G7 nanoparticles obtained by dynamic light scattering (DLS) are 37.7 and 45.9 respectively. The relaxivity values,  $r_1$  and  $r_2$ , for the SPIO-mPEG-8G7 measured at  $37.0 \pm 0.1$  °C and 20 MHz of are 24.97 and 206.01 mM<sup>-1</sup>s<sup>-1</sup>, respectively. The targeting ability of SPIO-mPEG-8G7 nanoparticles was confirmed by *in vitro* magnetic resonance imaging (MRI) study. SPIO-mPEG-8G7 nanoparticles show noticeable magnetic resonance contrast in phantom containing cell line expressing MUC4. In addition, graphene nanosheets (GNSs) were synthesized in high yield by MPCVD. The structure was characterized by scanning electron microscopy, transmission electron microscopy, selective area electron diffraction pattern, x-ray diffraction, and Raman spectroscopy. The experiments are in progress to develop pure carbon based  $T_2$  MRI contrast agent.

## Acknowledgements

I am under no illusion; completing my master project would not have been possible without support of others, and I am so grateful to a long list of people and the various roles they played. I would like to begin by expressing my deep gratitude to my advisor Prof. Y.M. Wang for introducing me to the area of molecular imaging and his inspiring and encouraging attitude toward me. I thank my committee member for their scientific guidance and input. I am also thankful to Mr. Ming Hung and Miss. Shaulin for their generous assistance.

I express my deepest gratitude to Mr. Manish Bhuban for love, affection and caring attitude he extended towards me and the specific thanks goes to Dr. J. N. Tiwari, he who showed me, the light at the end of dark tunnel

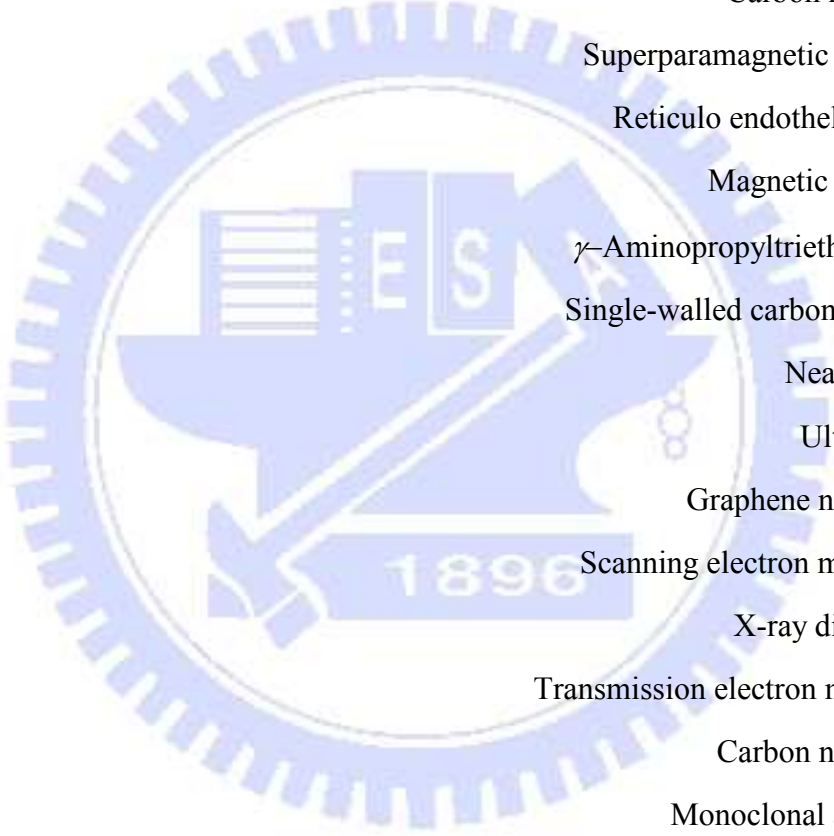
I would also like to acknowledge each and every moment of my life in Taiwan.



# Contents

Abstract (Chinese) -----	I
Abstract (English)-----	II
Acknowledgements -----	III
Contents -----	IV
Abbreviations -----	V
Table Captions-----	VII
Figure Captions -----	VII
Schemes -----	VIII
Chapters	
1. Introduction -----	1
1.1 Background -----	1
1.2 MUC4 as Pancreatic Cancer Tumor Maker -----	5
1.2.1 Background-----	5
1.2.2 MUC4 Mucin -----	5
1.2.3 Role of MUC4 in Cancer Development-----	8
1.2.4 Monoclonal Antibodies Targeting MUC4 -----	10
1.3 Contrast Agent -----	10
1.3.1 Background-----	10
1.3.2 Paramagnetic Agents -----	13
1.3.3 Superparamagnetic Agents -----	14
1.3.3.1 Superparamagnetism -----	14
1.3.3.2 SPIO Nanoparticle in Molecular Imaging-----	16
1.3.3.3 Recent Advancement in Superparamagnetic Agents -----	17
1.3.4 Carbon Based Material for Future MRI Contrast Agent -----	20
2. Experimental Section-----	25
2.1 Instruments and Reagents -----	25
2.1.1 Instruments -----	25
2.1.2 Reagents-----	26
2.1.3 Cell Culture Medium-----	26
2.2 Experimental Methods-----	27
2.2.1 Immobilization of 8G7 mAb on SPIO-mPEG-NH <sub>2</sub> -----	27
2.2.2 Measurement of Particle Size-----	27
2.2.3 Relaxation Time Measurement -----	27
2.2.4 <i>In vitro</i> MRI -----	28
2.2.5 Synthesis of Graphene Nanosheet-----	28
3. Result and discussion-----	29
3.1 Physical Characteristics of SPIO-mPEG-8G7-----	29
3.2 Relaxivity of SPIO-mPEG-8G7 -----	31
3.3 <i>In vitro</i> MRI -----	33
3.4 Structural Characterization of GNSs -----	34
4. Conclusion -----	40
5. References-----	41

## Abbreviations



CA 19-9	Carbohydrate antigen 19-9
MRI	Magnetic resonance imaging
NMR	Nuclear magnetic resonance
GdCAs	Gadolinium-based contrast agents
QDs	Quantum dots
CNTs	Carbon nanotubes
SPIO	Superparamagnetic iron oxide
RES	Reticulo endothelial system
MR	Magnetic resonance
APTES	$\gamma$ -Aminopropyltriethoxy silane
SWNT	Single-walled carbon nanotubes
NIR	Near-infrared
UV	Ultra-violet
GNSs	Graphene nanosheets
SEM	Scanning electron microscope
XRD	X-ray diffraction
TEM	Transmission electron microscopy
CNSs	Carbon nanoscrolls
mAbs	Monoclonal antibodies
mPEG	Methoxypoly(ethylene glycol)
kDa	Kilo Dalton
RT-PCR	Real-time polymerase chain reaction
RF	Radiofrequency
$T_1$	Longitudinal relaxation time
$T_2$	Transverse relaxation time
HFIs	Hyperfine interactions

EFG	Electric field gradient
$k_{ex}$	Water exchange rate
$\tau_R$	Rotational correlation time
DTPA	Diethylene triamine pentaacetic acid
MnDPDP	Manganese dipyriddyldiphosphate
$K$	Effective anisotropy constant
$M_s$	Saturation magnetization
$k_B$	Boltzmann's constant
SPM	Superparamagnetic
USPIO	Ultra small particles of iron oxide
CVD	Chemical vapor deposition
SWNTs	Single-walled carbon nanotubes
p-NPNN	$\gamma$ -phase p-nitrophenyl nitronyl nitroxide
MWNTs	Multi-walled nanotubes
MHz	Megahertz
PBS	Phosphate buffered saline
GaN	Gallium nitride
BCA	Bicinchoninic Acid
DLS	Dynamic light scattering
PyBop	(Benzotriazol-1-yloxy) tripyrrolidinophosphonium hexafluorophosphate,
HoBt	1-Hydroxybenzotriazole
GNSs	Graphene nanosheets
FESEM	Field-emission scanning electron microscopy
SAED	Selected-area electron diffraction
HRTEM	High-resolution transmission electron microscopy



## Table Captions

<b>Table 1</b> Expression of MUC genes in pancreatic adenocarcinoma by RT-PCR analysis--	7
<b>Table 2</b> Expression of MUC genes in chronic pancreatitis by RT-PCR analysis-----	8
<b>Table 3</b> Relaxation Times of Aqueous SWNT Solutions-----	23
<b>Table 4</b> Physical properties of MnFe <sub>2</sub> O <sub>4</sub> -----	29

## Figure Captions

<b>Figure 1</b> A: schematic representation of the modular structure of MUC4. B: schematic representation of MUC4 protein -----	6
<b>Figure 2</b> Role of MUC4 in Cancer development -----	9
<b>Figure 3</b> Important interaction and dynamic parameters defining the efficiency of MRI contrast agent-----	12
<b>Figure 4</b> Energy barriers from one stable magnetic configuration to other -----	16
<b>Figure 5</b> Magnetism-engineered iron oxide (MEIO) nanoparticles. TEM images of MnFe <sub>2</sub> O <sub>4</sub> (MnMEIO), Fe <sub>3</sub> O <sub>4</sub> (MEIO), CoFe <sub>2</sub> O <sub>4</sub> (CoMEIO) and NiFe <sub>2</sub> O <sub>4</sub> (NiMEIO). Scale bar, 50 Nm -----	18
<b>Figure 6</b> Systematic diagram of a FeCo/Gc nanocrystal -----	19
<b>Figure 7</b> Systematic representation of the formation of CNSs -----	21
<b>Figure 8</b> Carbon nanotube noncovalently functionalized by amphiphilic Gd(III) chalets -	22
<b>Figure 9</b> Systematic illustration of the mechanism for transforming GO nanosheets into carbon nanoparticles and nanotube following their ultrasonication in acid ---	23
<b>Figure 10</b> Distributions of hydrodynamic diameters for the SPIO-mPEG-NH <sub>2</sub> and SPIO-mPEG-8G7 -----	31
<b>Figure 11</b> <i>T</i> <sub>1</sub> relaxation time of SPIO-mPEG-8G7 -----	32
<b>Figure 12</b> <i>T</i> <sub>2</sub> relaxation time of SPIO-mPEG-8G7 -----	32
<b>Figure 13</b> (A) <i>T</i> <sub>2</sub> -weighted images of positive and negative cells for MUC4 expression after the treatment with or without 0.3 mM SPIO-mPEG-8G7 nanoparticles. The upper rows show cells without contrast agent treatment. The lower rows show cells treated with contrast agent. (B) colour map -----	33
<b>Figure 14</b> XRD patterns of GNS/spherical carbon/GaN sample -----	34
<b>Figure 15</b> Side- view FESEM image of the GNSs/spherical carbon/GaN; (B-C) plane-view FESEM images of the GNSs/spherical carbon/GaN sample at different magnification; (D) CNS -----	36
<b>Figure 16</b> (A) TEM image of the individual GNS and the corresponding SAED pattern is shown in the inset; (B) HRTEM of the individual GNS -----	37
<b>Figure 17</b> Raman spectrums of the GNSs/spherical carbon/ GaN Sample-----	39

## Scheme Captions

**Scheme 1** Conjugation of 8G7 mAb on the surface of SPIO-mPEG-NH<sub>2</sub>, PyBop (benzotriazol-1-yloxy) tripyrrolidinophosphonium hexafluorophosphate, HoBt 1-hydroxybenzotriazole ----- 30

**Scheme 2** BCA-Protein Reaction Mechanism----- 30



# Chapter 1

## Introduction

### 1.1 Background

Pancreatic cancer often referred as the “silent killer” due to its latent nature of progression. It is fourth male and fifth female leading cause of cancer-related deaths in the western world [1], 883 cases of pancreatic cancer death have been reported in Taiwan itself from 1990 to 1994 [2]. Most patients with pancreatic cancer do not develop symptoms until after the disease has metastasized and at the time of diagnosis, > 80% of patients have locally advanced or metastatic disease [3]. After diagnosis the overall median survival time is 2–8 months and in general 5 years survival rate of pancreatic cancer patients is just only 1 % [4]. The most widely used and best validated marker for pancreatic cancer is CA 19-9 [5]. However due to inadequate sensitivity and specificity European Group on Tumor Marker [6] and American Society of Clinical Oncology [7] discourage the use of CA 19-9 as a test for pancreatic cancer, especially for early forms of the disease. Modern radiological techniques of imaging and diagnostic cannot detect the early stage of this disease. Additionally several overlapping symptomatological characteristics have been observed between pancreatic adenocarcinoma and chronic pancreatitis, thereby, it is often very difficult to perceive the distinction between both pathological cases [8]. Therefore, there remains a critical need for the development of novel targeted bioimaging probes for accurate and early detection of pancreatic cancer. MUC4 is a high molecular weight O-glycoprotein expressed in various epithelial tissues including the trachea, colon, stomach, cervix, and lung [9]. Although, MUC4 aberrant

expression is reported in premalignant and malignant pancreatic lesions as well as in several pancreatic cancer cell lines with no detectable expression in the normal pancreas or chronic pancreatitis [10,11] making it attractive biological marker for pancreatic cancer. Recent study has shown that MUC4 exhibits, 91% sensitivity and 100 % specificity for early diagnosis of pancreatic cancer [12].

In the last two decades magnetic resonance imaging (MRI) has emerge as an advanced and most powerful tool for clinical diagnostic imaging. It has many potential advantages that other imaging modality does not offer for instance, noninvasive, radiation free technique. The physical principle behind MRI is nuclear magnetic resonance (NMR). NMR was discovered by Felix Bloch and Edward Purcell back in 1946 [13-15]. The NMR phenomenon is based on the fact that the atomic nuclei which possess a spin angular momentum interact with magnetic fields. In MRI the resonance of water protons is primarily used for diagnostic purposes since water constitutes about 63% of our bodies and the natural abundance of  $^1\text{H}$  isotope is 99.9%. The major disadvantage of MRI is its inherent low sensitivity. To enhance the quality of image contrast agents have been often used prior to MR imaging [16]. Primarily gadolinium-based contrast agents (GdCAs) have been used in MRI investigations which serve as a  $T_1$  agent.

Recent development in nanotechnology has made it possible to synthesize, characterize, and specifically tailor the functional property of nanoparticle for biomedical and diagnostic application. The unique properties and utility of nanoparticles arise by virtue of high surface to volume ratio, large percentage of surface atoms compare to bulk materials and the size of nanoparticles is comparable to biomolecules such as proteins

and polynucleic acids [17]. The most extensively-studied nanomaterials include quantum dots (QDs) [18], carbon nanotubes (CNT) [19], nanoshells [20], and paramagnetic nanoparticles [21]. These nanoparticles have size approximately 100 to 10000 times smaller than human cells, hence nanoscale particles can offer extraordinary interactions with biomolecules both on the surface of and inside cells [22].

Recently, superparamagnetic iron oxide (SPIO) nanoparticles have found widespread application in medicine, in particular as contrast agents in MRI. SPIO nanoparticles are the most commonly used  $T_2$  contrast agents in clinics. SPIOs have an important advantage compared to paramagnetic ions since each vectorized particle bears a huge magnetic moment, compared to a single targeted paramagnetic ion [23]. Consequently SPIO may potentially provide higher contrast enhancement in MRI than conventional paramagnetic Gd-based contrast agents. Initially SPIOs were developed as  $T_2$  agent due their large size and magnetic moment. However, recent study shows that SPIO nanoparticles with size less than 10 nm have excellent  $T_1$  enhancing properties [24]. Nanoparticles are usually nonspecifically taken up by the reticulo endothelial system (RES) [25] and the overall size of the nanoparticle can affect the specificity of nanoparticle to the organ (liver, spleen, or lymph node), non-targeted iron oxide nanoparticles have been used for liver [26], spleen [27], and lymph node imaging [28]. The advancement in understanding of the molecular biology of cancer has provided an enormous range of target for drug delivery.

In general, tissue or organ-specific nanoparticle contrast agents have two components: a biocompatible magnetic nanoparticle capable of altering the MR signal intensity and biological moieties that possess lock-and-key interactions, including those

observed in antibody-antigen and enzyme-substrate recognition. Surface modifications involving biomolecules, surface coverage is significantly important as is the ability for the immobilized molecules to retain their native conformations and binding profiles. One extremely useful route to postsynthetic modification of iron oxide nanoparticles is accessed by employing the common organosilane reagent,  $\gamma$ -aminopropyltriethoxy silane (APTES) [29].

Single-walled carbon nanotubes (SWNT) exhibit unique electrical and optical properties, including large Raman scattering cross-sections, near-infrared (NIR) fluorescence, and UV/visible/NIR absorption [30-32]. It is an upcoming potent candidate for the photothermal therapeutic agent since it generates significant amounts of heat upon excitation with near-infrared light (NIR,  $\lambda=700-1100$  nm). Such a photothermal effect can be employed to induce thermal cell death in a noninvasive manner [33]. SWNT/iron oxide nanoparticle complexes have been used as multimodal biomedical imaging agents [34]. Recent studies have shown that quantum size effects cause finite CNTs to exhibit special properties such as magnetism [35].

The aim of this study was to develop  $T_2$ -weighted MRI contrast agent for early diagnosis of pancreatic cancer. For this study SPIO nanoparticle was generously gifted by Mr. Ming Hung. Synthesis and characterization methods of SPIO nanoparticle are beyond the scope of the thesis. In addition we have successfully synthesized graphene nanosheets (GNSs) in high yield. The GNSs have been characterized by scanning electron microscope (SEM), *X-ray diffraction* (XRD), Transmission electron microscopy (TEM), and Raman shift. The carbon nanoscrolls (CNSs) synthesized from GNSs has been observed by SEM. Experiments are in progress to evaluate saturation magnetization and  $T_2$  relaxation times

of CNSs. The 8G7 (anti-*MUC4* mAbs) was immobilized on the surface of SPIO nanoparticle which can specifically target abruptly expressed MUC4 mucine in pancreatic tumor. Typical hydrodynamic size distribution, relaxivity, and in vitro MRI study was conducted to evaluate sensitivity of SPIO-mPEG-8G7 nanoparticle.

## **1.2 MUC4 as Pancreatic Cancer Tumor Marker**

### **1.2.1 Background**

Mucins are proteins, which carry a large amount of sugar attached through oxygen (O-linked) to the protein core. The epithelial mucins are expressed by the cells that line the tubes and glands in some tissues of the body, for example the stomach, colon and ducts of the breast [36]. In general, musines are involved in the protection and lubrication of epithelial surfaces. However, recent study shows that mucins are also involved in cell signaling modulation and affect tumor cell phenotype [37].

### **1.2.2 MUC4 Mucin**

MUC4 is a high molecular weight transmembrane mucin that is expressed by various epithelial cells (trachea, lung, stomach, colon and cervix) in normal tissues [38]. MUC4 has two subunits, MUC4 $\alpha$  and MUC4 $\beta$ . The two subunits are non-covalently link to each other. Schematic representation of the modular structure of MUC4 is shown in Figure 1. The mucin type subunit MUC4 $\alpha$  is of 850 kDa and the membrane-bound growth factor like subunit of 80 kDa [39]. Numerous studies have established association of MUC4 with the progression of cancer and metastasis. An aberrant expression of MUC4 is reported in precancerous lesions, indicating its early

involvement in the disease process with no detectable expression in the normal pancreas or chronic pancreatitis [40].

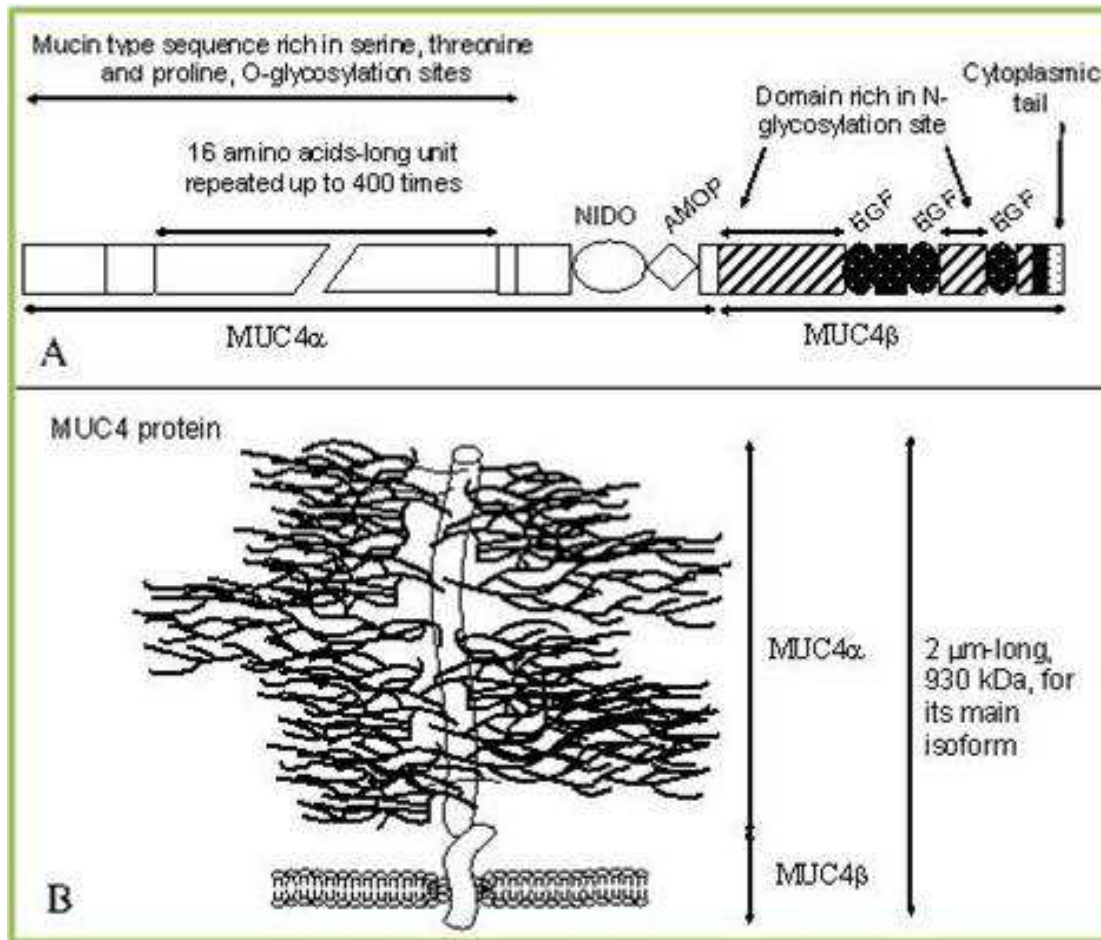


**Figure 1** A: Schematic representation of the modular structure of MUC4. B: Schematic representation of MUC4 protein. The representation is not drawn to scale. [39]

The RT-PCR analysis of MUC genes expression in pancreatic adenocarcinoma and chronic pancreatitis are shown in Table 1 and Table 2 respectively. Overlapping symptomatological characteristics have been observed between pancreatic adenocarcinoma and chronic pancreatitis [8]. However from the Table 1 and Table 2 we can easily observe that, in pancreas aberrant expression of MUC4 gene exclusively occurs



during pancreatic adenocarcinoma making it novel biomarker for diagnosis of pancreatic cancer.

**Table 1** Expression of MUC genes in pancreatic adenocarcinoma by RT-PCR analysis<sup>a</sup>. Total RNA from 15 pancreatic tumor cell lines was isolated and subjected to semiquantitative RT-PCR<sup>a</sup>

Cell lines	DS <sup>b</sup>	Expression level <sup>c</sup>							
		MUC1	MUC2	MUC3A	MUC4	MUC5AC	MUC5B	MUC6	MUC7
SC2P9	WD	+	++	-	+++	++	-	-	-
Capan 1	WD	+++	+++	-	++++	+++	+++	+++	-
Capan 2	WD	++	-	-	++++	-	-	-	-
HPAF	WD	+++	+	-	++++	+++	++	-	-
Panc1	PD	+	-	-	-	++	+++	-	-
ASPC-1	ND	+++	-	-	++	-	+++	-	-
HCG25	PD	+++	-	-	-	-	-	-	-
T3M4	MD	++	+++	-	+++	-	+	-	-
Colo357	WD	++++	-	-	+++	++	+++	-	-
BxPC3	MD	+++	++	-	+++	-	+	+++	-
MiaPaCa	ND	+	-	-	-	-	-	-	-
HPAC	ND	++++	-	-	+++	++	-	-	-
QGP1	ND	+	-	-	+++	-	-	-	-
HS766T	ND	+	+	-	-	+++	++	++	-
Panc89	MD	ND	++	-	+++	++	++	-	-
Pancreasc <sup>d</sup>		+++	-	-	-	+++	+++	++++	-
Tracheac <sup>d</sup>		++	++	-	+++	++++	++++	-	-
S.I. <sup>d</sup>		+	++++	++++	+	-	-	++++	-
S.G. <sup>d</sup>		ND	-	-	+++	-	++	-	++++

<sup>a</sup>Data obtained from reference [40]. <sup>b</sup> D.S., differentiation stage; PD, poorly differentiated; MD, moderately differentiated; WD, well differentiated; ND, not determined. <sup>c</sup> -, no expression; +, low level; ++, moderate level; +++, high level; +++++, very high level; ND, not determined. <sup>d</sup> Normal tissue samples were included as controls. S.I., small intestine; S.G., salivary gland

**Table 2** Expression of MUC genes in chronic pancreatitis by RT-PCR analysis<sup>a</sup>. Total RNA from 10 chronic pancreatitis samples was isolated and subjected to semiquantitative RT-PCR.

Sample	Expression level <sup>a</sup>							
	MUC1	MUC2	MUC3A	MUC4	MUC5AC	MUC5B	MUC6	MUC7
1	+	-	-	-	-	++++	++	-
2	+	-	-	-	-	+++	++	-
3	+	-	-	-	-	-	++	-
4	+	-	-	-	++	++	++++	-
5	+	-	-	-	-	++	++	-
6	+	-	-	-	-	+	++	-
7	+++	-	-	-	-	++	++	-
8	+	-	-	-	-	+	++++	-
9	+	-	-	-	-	++	+++	-
10	+	-	-	-	-	++	++	-

<sup>a</sup>Data obtained from reference [40]. <sup>b</sup> -, no expression; +, low level; ++, moderate level; +++, high level; +++++, very high level.

### 1.2.3 Role of MUC4 in Cancer Development

During cancer development controlled interaction between neighboring cells and the cell and the extracellular matrix are interrupted, whereas new interactions establish due to alterations in the cell surface proteins, extracellular matrix composition, and loss of cell polarity. A favorable environment is created by these molecular and cytoarchitectural changes at the tumor site which facilitate in tumor development [41]. The MUC4 is a multifunctional protein implicated in a variety of biological functions. Under normal conditions, MUC4 is localized at the apical surface of the epithelial cells. Genetic/epigenetic changes, alternative splicing, and biochemical modifications may result in an aberrant expression of MUC4 [12]. In addition, MUC4 can change the role of other adhesion-associated signaling molecules *via* steric hindrance. Lose in polarity of tumor cell, facilitate MUC4 to find new interacting partner(s). Recent studies established

that MUC4 interacts with HER2/ ErbB2 and alter its expression [41]. Role of MUC4 in cancer development is systematically shown in Figure 2.

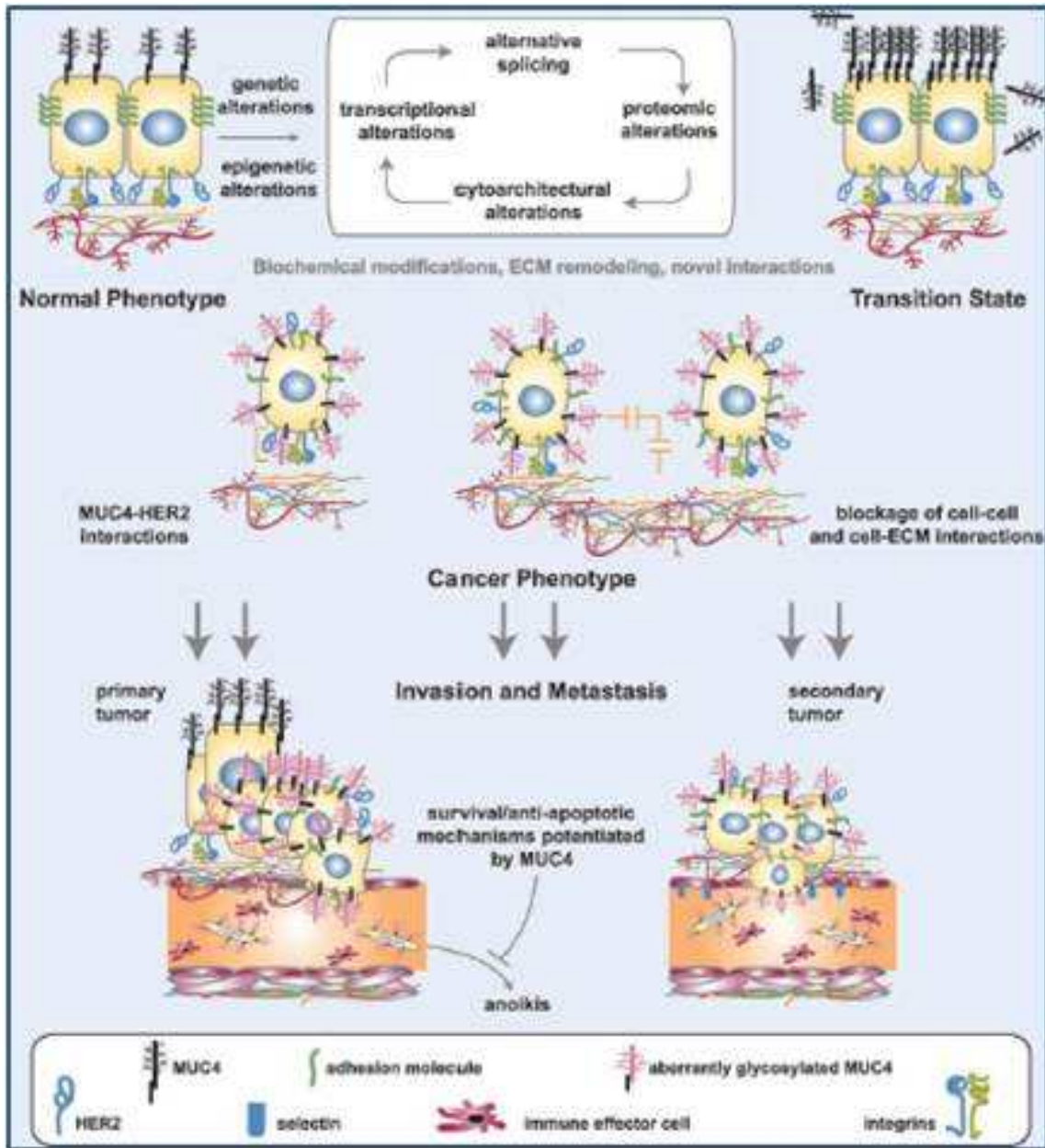


Figure 2 Role of MUC4 in cancer development [12]

## **1.2.4 Monoclonal Antibodies Targeting MUC4**

The overriding challenge in developing antibodies to specifically target mucin proteins is lies in their structure, 80% of their mass is composed of glycan chains. The Glycan chains cover greater part of the core protein epitopes. The main mucin-type antibodies available recognize glycan epitopes and therefore do not bind with a unique mucin. For instance, the DU-PAN-2 antibody is reactive with MUC1 and MUC4 [40]. Recently, a series of monoclonal antibodies (mAbs), 9H8-1F3, 13F12-2C9, 12B8-2D9, 8G7-1D1, 12C11-1G2, 11A8-1B7, and K2G6-1H6, directed against the TR region of MUC4 have been reported [38]. To generate these antibodies a 16-amino-acid sequence was chosen same as that of 16 amino acid residues repeated in tandem up to 400 times for the main MUC4 allele [42]. The mAb, 8G7 has been discovered to strongly react against the MUC4 peptide and with native MUC4 from human tissues or pancreatic cancer cells in Western blotting, immunohistochemistry, and confocal analysis [38].

## **1.3 Contrast Agent**

### **1.3.1 Background**

It had been known long back that atomic nuclei, which possess a spin angular momentum, will interact with magnetic field. In 1971, Raymond Damadian observed that certain mouse tumors display high relaxation times compared with normal tissue and this was the was the inception of imaging the human body [43]. MR signal is due to relaxation of water protons that are trying to realign with a static magnetic field following the application of radiofrequency (RF) pulse. In 1948, Bloch et al. reported the use of the paramagnetic ferric nitrate salt to enhance the relaxation rate of water proton. Three

decades later Lauterbur et al. applied Mn(II) salt to distinguish between different tissue based on the differential relaxation time and thus produce the first MR image [44]. Extensive application of MRI in clinical imaging and biomedical research has promoted the development of a new class of pharmacological product, called contrast agent. It acts as catalyst in shortening the longitudinal and transverse (i.e.,  $T_1$  and  $T_2$ ) relaxation time of water protons in tissue in which the agent accumulates, consequently, enhances the image contrast between normal and diseased tissue and indicate the status of organ function or blood flow. Currently, 30% of all MRI examinations worldwide are performed with contrast agents [45].

The efficiency of an MRI contrast agent can be quantified by its relaxivity,  $r_1$ , which is defined as the increase of the longitudinal relaxation rate of the water protons per mM of the paramagnetic compound. Relaxivity can be expressed as function of two sets of parameters.

$$r_1 = f\left(\left\{A_{iso}, \overset{\leftrightarrow}{T}, \overset{\leftrightarrow}{Q}, \dots\right\}, \left\{k_{ex}, T_{1e}, T_{2e}, \tau_R, \dots\right\}\right)$$

The first set of parameters is responsible for interactions of nuclear spins with electron surrounding and second set of parameters in equation is responsible for the dynamic part. Most important interactions which influence the paramagnetic relaxation enhancement are, Fermi contact ( $A_{iso}$ ) and the dipolar ( $\overset{\leftrightarrow}{T}$ ) hyperfine interactions (HFIs), i.e. the magnetic interaction between the spins of nuclei and electrons. Coupling tensor,  $\overset{\leftrightarrow}{Q}$ , i.e. The interactions of nuclear quadrupoles with the electric field gradient (EFG) are

important for the description of relaxation of nuclei with a spin number larger than 1/2, for instance  $^{17}\text{O}$  nuclei [46]. The important dynamic parameters (second part of eq. 4) that influence the paramagnetic relaxation are the exchange rate between the bound water molecules and the bulk water,  $k_{ex}$ , the longitudinal and transverse electronic relaxation times,  $T_{1e}$  and  $T_{2e}$ , and the rotational correlation time  $\tau_R$  [46]. These parameters are schematically summarized in Figure 3.

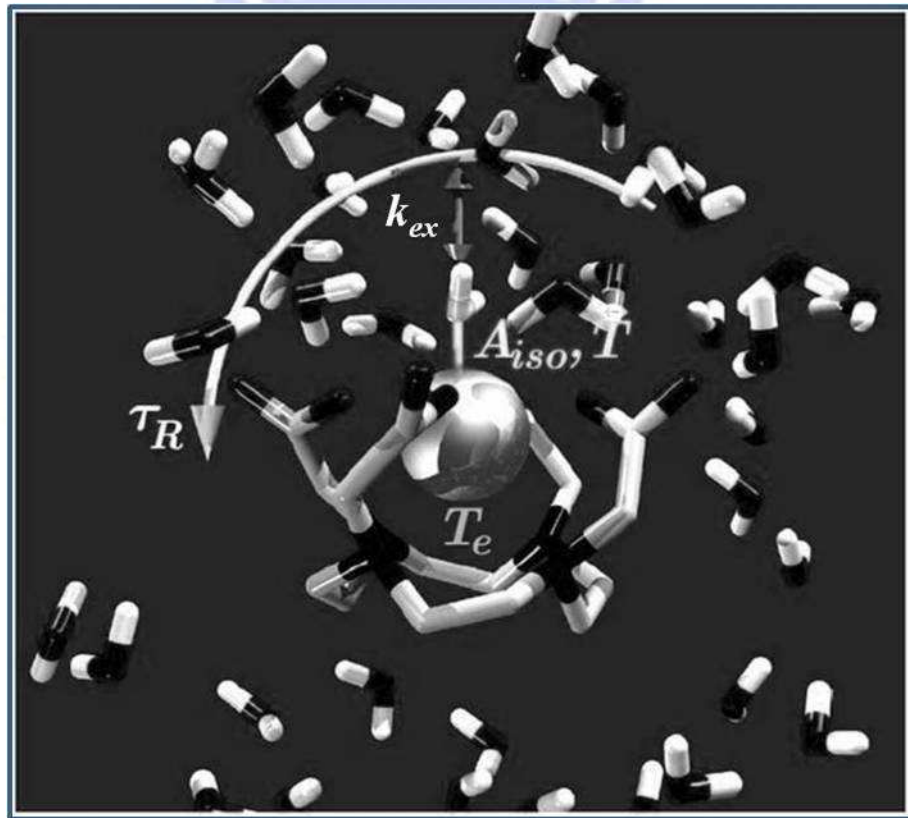


**Figure 3** Important interaction and dynamic parameters defining the efficiency of an MRI contrast agent.

### 1.3.2 Paramagnetic Agents

Metal ions with one or more unpaired electrons are paramagnetic, paramagnetism is due to the spin and orbital angular momentums of unpaired electrons, and therefore have a permanent magnetic moment. However, the magnetic moments of individual paramagnetic atoms in a material are only weakly coupled to each other, and room temperature thermal energy is sufficient to overcome these interactions to eliminate any net magnetic moment [47]. A small fraction of the atomic moments aligns parallel to the field in accord with the Boltzmann distribution when placed in a magnetic field. The paramagnetic interaction with the field is weak and disappears in the absence of an applied field [48]. In an aqueous solution of paramagnetic metal, there is a dipolar magnetic interaction between the electronic magnetic moment of the paramagnetic atom and much smaller magnetic moments of the protons in its vicinity belonging to water molecules. Random fluctuations in this dipolar magnetic interaction, mainly a result of molecular motions, reduce both the longitudinal ( $T_1$ ) and transverse ( $T_2$ ) relaxation of water proton [49]. Gadolinium (Gd(III)) and manganese (Mn(II)) are paramagnetic ions which have been successfully used in MR contrast agents. The Gd(III) ion is an ideal paramagnetic metal ion for MRI contrast agent. The Gd(III) is an ideal choice as a paramagnetic ion is for several reasons. First of all, this ion is characterized by a large magnetic moment due to the half-filled  $4f$  shell (7 unpaired electrons!). Secondly, due to the symmetric  $S$  state this ion has a relatively long electron spin relaxation time which is one of the necessary requirements for efficient paramagnetic relaxation enhancement. However Gd(III) cannot be used as contrast agents in their ionic form due to an undesirable biodistribution and the relatively high toxicity [50]. Therefore, ligands have

been designed that can form stable complexes with paramagnetic metal ions to form strong chelates which can remain stable in the body and thereby significantly reducing toxicity. The Gd(III) coordinate strongly to diethylenetriamine backbones modified with carboxylic acids. In complexes with such ligands the ion is normally nine-coordinate, with seven or eight coordination sites occupied by the ligand. One or two sites in the coordination sphere of the ion are occupied by water molecules. The role of this water molecule is crucial for the efficiency of MRI contrast agent since its nuclear spins are strongly influenced by the magnetic moment of the neighbor Gd(III) ion. The Gd(III)-diethylenetriamine pentaacetic acid (Gd-DTPA, Magnevists) is the first Gd(III)-complex approved for clinical use. Subsequently, many derivatives of DTPA and other chelates were introduced. Since the approval of  $[\text{Gd}(\text{DTPA})(\text{H}_2\text{O})]^{2-}$  in 1988, it is estimated that over 30 metric tons of gadolinium have been administered to millions of patients worldwide [45]. Mn(II) complexes have also been investigated for its potential application in MRI. However due to poor stability it is not used as widely as Gd(III) complexes. Consequently so far, MnDPDP (Teslascant) in which Mn(II) is coordinated by dipyradoxyl diphosphate, is the only clinically approved agent [51].

### **1.3.3 Superparamagnetic Agents**

#### **1.3.3.1 Superparamagnetism**

In general, macroscopic ferromagnetic materials are divided up into domains of parallel magnetic moments for minimization of their energy. Within a magnetic domain, the magnetic moments orient in one direction, while the alignment of spins in neighboring domains is usually antiparallel. The oppositely aligned magnetic domains are separated



from each other by a domain wall (Bloch wall). As the particle size decreases below some critical value, the formation of domain walls become energetically unfavorable and the ferromagnetic particle can support only a single domain structure. The critical diameter for a magnetic particle to reach the single domain limit is equal to [52]

$$R_{sd} = \frac{36\sqrt{AK}}{\mu_o Ms^2}$$

where  $A$  is the exchange constant,  $K$  is the effective anisotropy constant and  $M_s$  is the saturation magnetization. Magnetic particles of nanometer size are usually in a single domain structure [53]

The amount of energy required to reverse the magnetization of a single domain particle, over the energy barrier from one stable magnetic configuration to the other is proportional to  $KV/k_B T$  where  $V$  is the particle volume,  $k_B$  is Boltzmann's constant and  $T$  is temperature [54]. In zero magnetic fields, the energy barrier  $\Delta E$  has to be overcome to rotate the magnetization of a single-domain particle as shown in Figure 4. Because the height of the barrier,  $\Delta E = KV$ , is proportional to the particle volume  $V$ ,  $\Delta E$  may become comparable to the thermal energy ( $k_B T$ , where  $k_B$  shows the Boltzmann's constant) when the particle size decreases. If the thermal energy is large enough to overcome the anisotropy energy so that the energy barrier can no longer pin the magnetization to the time scale of observation, the magnetization is no longer stable due to thermal fluctuations and the particle is said to be superparamagnetic (SPM) [55].

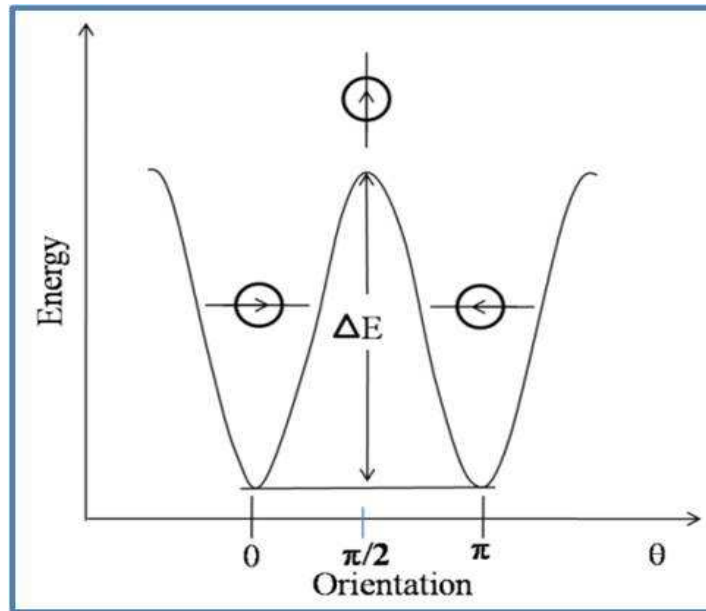


**Figure 4** Energy barriers from one stable magnetic configuration to the other

### 1.3.3.2 SPIO Nanoparticle in Molecular Imaging

Molecular imaging, in general, refers to the study of cellular and molecular events through noninvasive investigation. In MRI, molecular imaging depends on induced changes in proton relaxivity of in vivo water molecules on the molecular and cellular level. In last one decade, biocompatible iron oxide particles conjugated with targeting moiety for targeted molecular imaging applications has been extensively investigated. Monoclonal antibodies labeled with superparamagnetic nanoparticles are expected to be good tumor-specific contrast agents because of their high specificity against some cancers. Superparamagnetic iron oxide nanoparticles (SPION) are currently used for clinical imaging of liver tumors and prostate, breast and colon cancers as well as for the delineation of brain tumor volumes and boundaries.

### 1.3.3.3 Recent Advancement in Superparamagnetic Agents

Magnetic nanoparticle probes are emerging as a next generation contrast medical imaging. Super paramagnetic iron oxide (SPIO) particles were suggested as potential liver specific MR contrast agents as early as the mid 1980s [56]. Recent research shows SPIO particles have potentially to generate higher contrast enhancement in MRI than conventional paramagnetic Gd-based contrast agents. Numerous chemical methods have been reported for synthesise of SPIO nanoparticles for medical imaging applications: microemulsions [57], sol-gel syntheses [58], sonochemical reactions [59], hydrothermal reactions [60], hydrolysis and thermolysis of precursors [61], flow injection syntheses [62], and electrospray syntheses [63]. Aqueous co-precipitation process in the presence of the coating material has been frequently employed for the synthesis of SPIO and USPIO. The main advantage of this process is that a large amount of nanoparticles can be synthesized. However, the control of particle size distribution is limited, because only kinetic factors are controlling the growth of the crystal [64-66]. The saturation magnetizations ( $M_s$ ) Values of nanoparticles obtained by these methods are in the range of 30–50 emu/g, which is lower than the 90 emu/g reported for their bulk form. The low  $M_s$  value is due to incorporation of impurities hampering the crystal structure and surface effect [67]. Monodisperse magnetite nanoparticles has been synthesized at high-temperature by decomposition reaction of iron(III) acetylacetonate with 1,2-hexadecanediol in the presence of oleic acid and oleylamine to. The particle diameter can be tuned from 4 to 20 nm by varying the reaction temperature [68]. However, use of hydrophobic oleic acid and oleylamine surfactants in the process results in a hydrophobic coating on the particle surface, amphiphilic polymer or surface surfactant exchange have been utilized to overcome this problem [69]. In order to meet the demand of excellent

magnetic property for the applications such as, molecular imaging, metal doped iron oxide nanoparticles have drawn much attention due to their enhanced magnetic properties. Spinel metal ferrites with a composition of  $MFe_2O_4$ , where M is +2 cation of Mn, Fe, Co or Ni, have been fabricated by various methods to tune specific magnetic properties. Comprehensive study conducted by Lee *et al.* on 12 nm ferrite nanoparticles ( $MnFe_2O_4$ ,  $Fe_3O_4$ ,  $CoFe_2O_4$ ,  $NiFe_2O_4$ ) for MRI application shows that 12 nm  $MnFe_2O_4$  NPs have the highest mass magnetization value of 110 (emu per mass of magnetic atoms) among  $MnFe_2O_4$ ,  $Fe_3O_4$ ,  $CoFe_2O_4$ ,  $NiFe_2O_4$  as shown in Figure 5. Furthermore their results also suggest that  $MnFe_2O_4$  nanoparticles are nontoxic in vitro and possess higher magnetic susceptibility than magnetite nanoparticles, suggesting that they may be used as an ultrasensitive MR imaging probe [70].

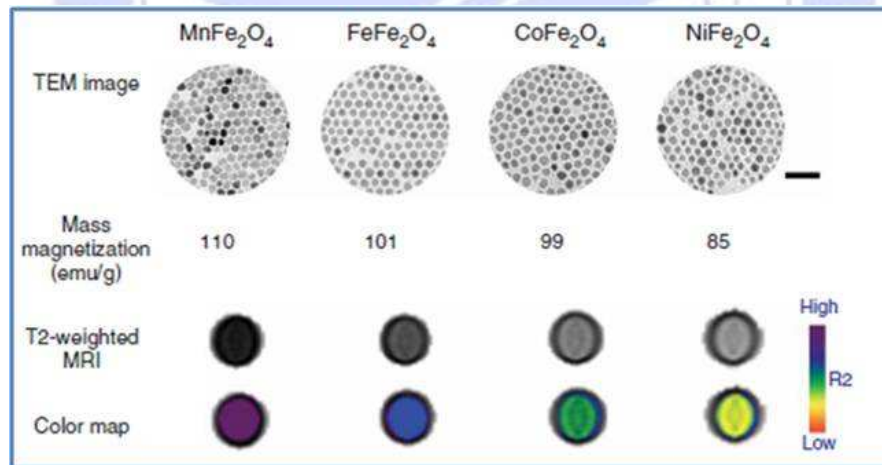


**Figure 5** Magnetism-engineered iron oxide (MEIO) nanoparticles. TEM images of  $MnFe_2O_4$  (MnMEIO),  $Fe_3O_4$  (MEIO),  $CoFe_2O_4$  (CoMEIO) and  $NiFe_2O_4$  (NiMEIO). Scale bar, 50 nm<sup>[70]</sup>

Recently, Seo *et al.* reported synthesis of bimetallic FeCo core of 7 nm and 4 nm with a single-graphitic shell through chemical vapor deposition (CVD), a systematic graphical

design shown in Figure 6. The  $M_s$  of the 7 nm and 4 nm nanocrystals were 215 emu/g and 162 emu/g, respectively with excellent  $r_1$  and  $r_2$  relaxivities [24].

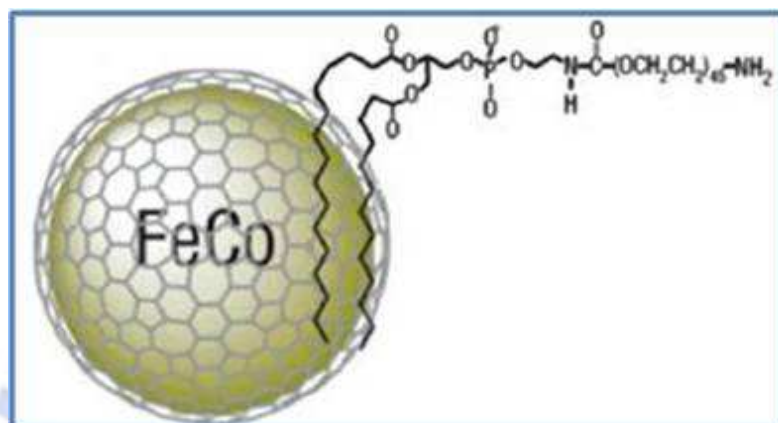


**Figure 6** Systematic diagram of a FeCo/GC nanocrystal [24]

The direct use of SPION as in vivo MRI contrast agents results in biofouling of the particles in blood plasma and formation of aggregates due to high surface energy that triggered by the “opsonization” process resulting in fast clearance of SPIO nanoparticles [71]. Therefore, it is essential to engineer the surface of the SPION to minimize biofouling and aggregation of the particles in physiological conditions for long periods. Poly (ethylene glycol) (PEG) is widely used polymer for nanoparticle coating. Kohler *et al.* developed bifunctional PEG silanes capable of forming self-assembled monolayers (SAMs), furthermore terminal functional group (amine or carboxyl) extending out from the nanoparticle surface provide sites for conjugation of functional ligand.

### 1.3.4 Carbon Based Materials for Future MRI Contrast Agent

In last two decades a wide range of all-carbon nanostructures have been discovered for instance, fullerenes (1985), carbon nanotubes (1991), graphene (2004). Since the discovery of carbon nanotube (CNT) in 1991 [72], it has been used extensively used for various technological applications [73-74]. Chemically modifiable outer surface have been used as diagnostic and therapeutic agents in medicine [75-76]. Single-walled carbon nanotubes (SWNTs), fabricated from single sheets of graphene have been extensively investigated forms of carbon nanotubes for biological and medical and other technological application owing to its intriguing physical properties such as quantum electronic transport [77], a tunable band gap [78], extremely high mobility [79], high elasticity [80] and electromechanical modulation [81].

Although there has been doubt as to whether the ferromagnetic features of some of the graphitic materials was due to magnetic impurities such as iron. Recent study shows occurrence of intrinsic magnetism in carbon-based materials possessing the  $sp^2$  network [82]. Carbon-based magnetic materials would bring a new prospective to technologies relying on magnetism for instance MR imaging. Surprisingly, the first organic ferromagnet, the  $\gamma$ -phase p-nitrophenyl nitronyl nitroxide (p-NPNN) was discovered only in 1991 [83]. Such materials may have low density, be transparent or environment-friendly.

Graphene, a two-dimensional honeycomb lattice of  $sp$ -bonded carbon atoms, has shown a wealth of exceptional properties. Since the discovery of the first isolated graphene in 2004, it has attracted major interest, because of its high charge mobility and crystal quality [84]. Xie *et al.* and Yu *et al.* have reported synthesis of carbon nanoscrolls

[85] and carbon nanotube [86] from monolayer graphene respectively. Schematic representation of CNS formation is shown in Figure 7.

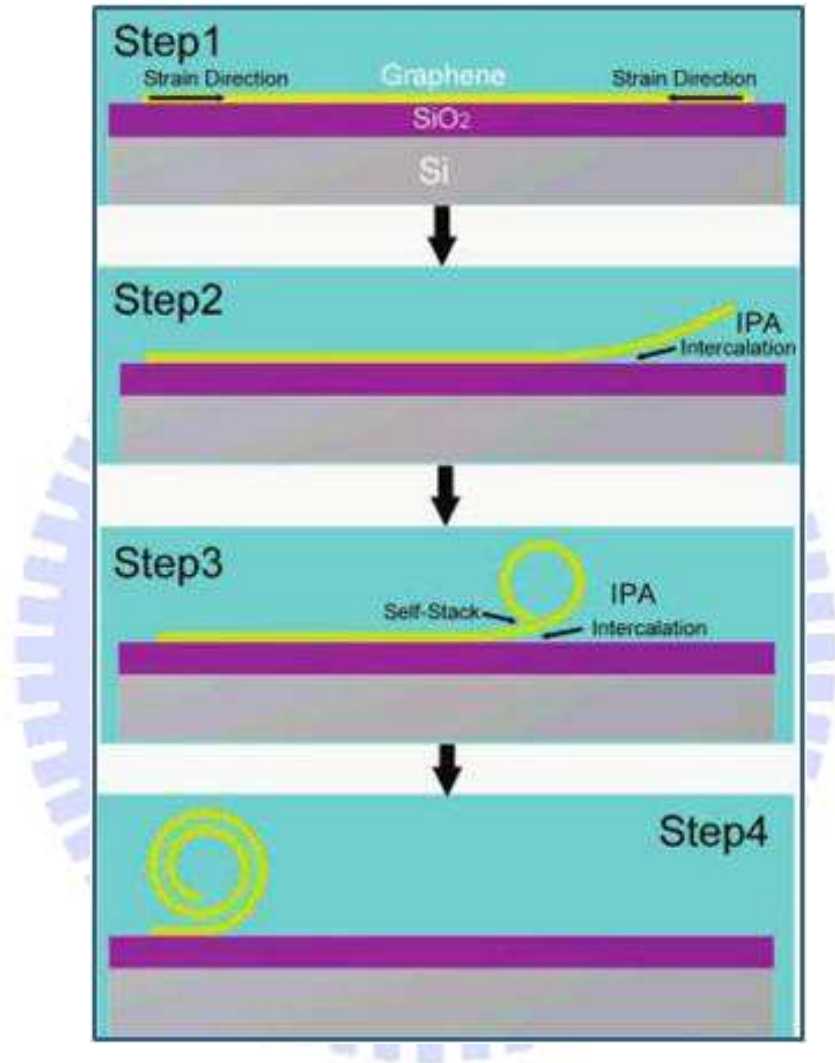


**Figure 7** Schematic representation of the formation of CNS. Step1: surface strain is induced in graphene after it is immersed in IPA solution. Step2: the edge of graphene is lifted up with the help of the surface strain and the intercalation of IPA solution. Step3: the initial bending of the graphene is energetically unfavorable and might be caused by perturbations. Once the graphene gets selfstacked, the scrolling process will be easier. Step4: the graphene continued to roll up until a CNS is formed.<sup>[85]</sup>

Richerd *et al.* have reported noncovalent functionalization of carbon nanotube with amphiphilic Gd(III) chelates, a systematic scheme shown in Figure 8. The study shows  $T_2$  frequencies at any GdL concentration are remarkably lower than that of pure water, and they are practically independent of both the frequency and the Gd(III) concentration (8.5-13.8 ms for MWNT/GdL versus 2500 ms for water). Interestingly, the transverse relaxation times,  $T_2$  values of suspensions containing MWNT and the amphiphilic ligand L at various concentrations without any Gd(III) are in the same range as those measured in the solutions containing Gd(III) [87].

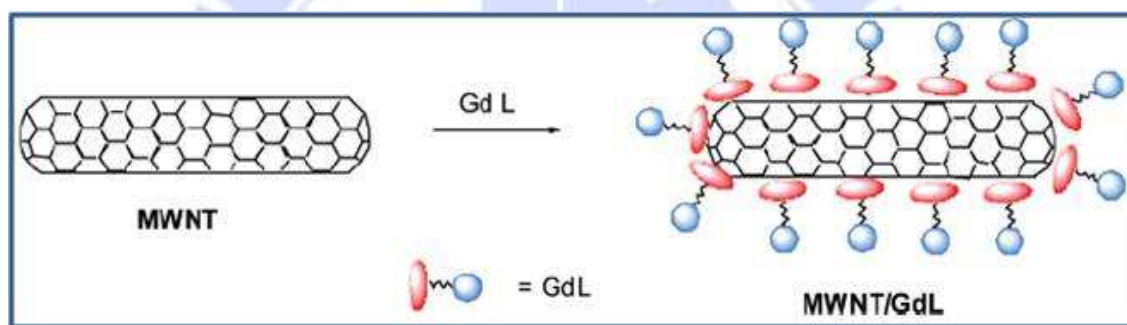


**Figure 8** Carbon nanotubes noncovalently functionalized by amphiphilic Gd<sup>3+</sup> chelates<sup>[87]</sup>

Recently, Ananta *et al.* have report that raw HiPco SWNTs (r-SWNTs), purified SWNTs (p-SWNTs), and US-tubes show inherently high performance  $T_2$ -weighted MRI contrast agents by virtue of their superparamagnetic character, with the US-tubes being the most efficacious of the materials by far. The high-efficacy contrast performance is due to contributions from both the iron catalyst nanoparticles (originating from the synthesis of SWNT materials) and the carbon SWNT material itself. Table 3 shows relaxation time of Aqueous SWNT solution along with clinically-used SPIO (Ferumoxtran)  $T_2$  agent measured at 1.41 T and 37 °C [88].



**Table 3** Relaxation Times of Aqueous SWNT Solutions (dispersed using pluronic surfactant)<sup>a</sup>

sample	[Fe] mM	$T_1$ (ms)	$T_2$ (ms)	$r_1$ (mM <sup>-1</sup> s <sup>-1</sup> ) <sup>b</sup>	$r_2$ (mM <sup>-1</sup> s <sup>-1</sup> ) <sup>b</sup>	$r_2/r_1$	$T_2$ (ms · mg <sup>-1</sup> ) <sup>c</sup>
r-SWNT	0.449		34.6		63.6		4.6
p-SWNT	0.167	242.2	46.5	22.8	126.8	5.6	5.1
US-tube	0.075	1000	67.7	8.9	192.5	21.6	31.7
Ferumoxtran-10				9.9	65	6.6	

<sup>a</sup>Data were collected with a Bruker Minispec Mq-60 spectrometer at 1.41 T and 37 °C. For comparison, a clinically-used SPIO  $T_2$  agent (Ferumoxtran) is also included. <sup>b</sup> Based on the Fe concentration. <sup>c</sup> Based on the SWNT concentration [88]

Wang *et al.* has reported synthesis of soluble carbon nanotubes by the sonication of graphene oxide nanosheets. Systematic diagram of synthesis procedure is depicted in Figure 9.

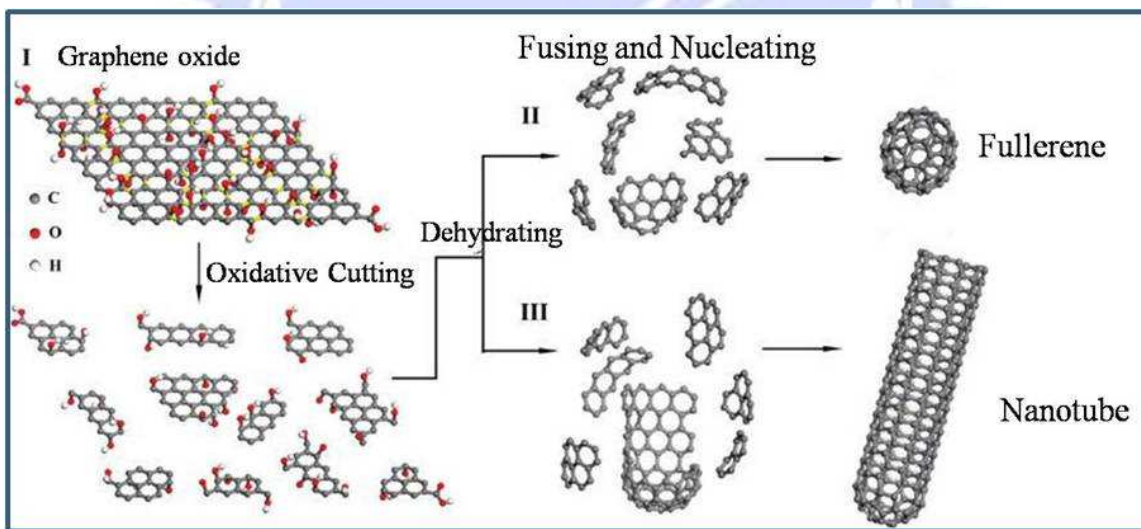
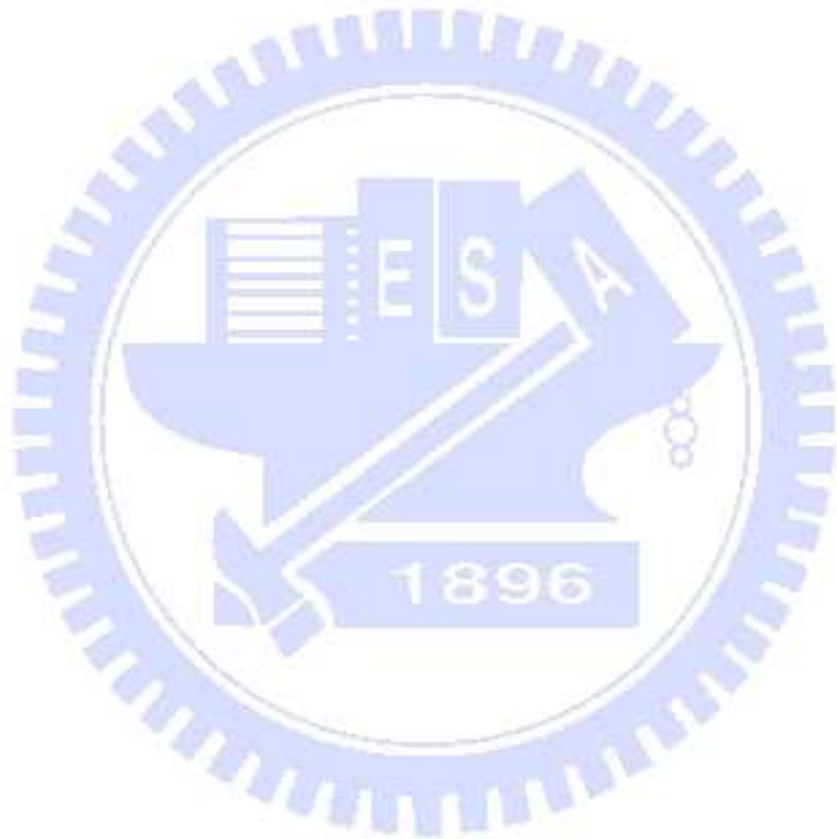


**Figure 9** systematic illustration of the mechanism for transforming GO nanosheets into carbon nanoparticles and nanotubes following their ultrasonication in acid. (I) Oxidative cutting of graphene oxide produces PAH molecules in concentrated HNO<sub>3</sub>. In the dehydrating acidic medium, the polyaromatic fragments fuse and nucleate into (II) carbon nanoparticles or (III) nanotubes via acid-catalyzed intramolecular or intermolecular dehydration reactions. [89]

The saturation magnetization of CNT synthesized by Wang *et al.* increased from 25  $\mu\text{emu cm}^{-2}$  to a maximum of 100  $\mu\text{emu cm}^{-2}$  upon annealing to 400 °C and gradually dropped to 41  $\mu\text{emu cm}^{-2}$  on annealing at higher temperatures [89].



# Chapter 2

## Experimental Section

### 2.1 Instruments and Regents

#### 2.1.1 Instruments

1. Particles diameter analyzer (Dynamic Light Scattering): English Malvern Instruments Company, Model: ZetaSizer 3000 HAS
2. NMR relaxometer (NMS-120 Minispec, Bruker)
3. CO<sub>2</sub> incubator (Japan SANYO, Model: MCO-20AIC)
4. MR scanner (3.0 T) (Sigma; GE Medical Systems, Milwaukee, WI)
5. MPCVD (ASTeX type microwave plasma CVD)
6. XRD
7. Field-emission scanning electron microscopy (FESEM, JEOL JSM-6700F)
8. Transmission electron microscope (Philips TEM)
9. Raman microscopy (LABRAMHR).

## 2.1.2 Reagents

### 1. Zymed Laboratories:

Mouse anti- MUC4, clone 1G8

### 2. HyClone :

RPMI-1640 medium

### 3. Mallinckrodt

Methanol 99.7 %

### 4. TEDIA :

Dimethyl sulfoxide ( DMSO ) 99.9 %

### 5. GIBCO:

Dulbecco's modified Eagle's medium

## 2.1.3 Cell Culture Medium

Culture Medium for BxPC-3

RPMI 1640 medium with 2 mM L-glutamine adjusted to contain 1.5 g/L sodium bicarbonate, 90%; fetal bovine serum, 10%

Culture Medium for PANC-1

90% Dulbecco's modified Eagle's medium with 4 mM L-glutamine adjusted to contain 1.5 g/L sodium bicarbonate and 4.5 g/L glucose + 10% fetal bovine serum

## 2.2 Experimental Methods

### 2.2.1 Immobilization of 8G7 mAb on SPIO-mPEG-NH<sub>2</sub>

One hundred microliters of the SPIO-mPEG-NH<sub>2</sub> at a concentration of 4 mg Fe/mL was added to 400 IL of 8G7 mAb (ZYMED Laboratories, UK), using 1-hydroxybenzotriazole and (benzotriazol-1-yloxy) tripyrrolidinophosphonium hexafluorophosphate as catalysts, and the mixture was stirred for 24 h at room temperature. The solution was separated from unbound 8G7 mAb by dialysis.

### 2.2.2 Measurement of Particle Size

The hydrodynamic diameter of the SPIO-mPEG-NH<sub>2</sub> particles was measured using a Zetasizer Nano-z (Malvern Instruments, Malvern, UK) through dynamic light scattering (DLS).

### 2.2.3 Relaxation Time Measurement

The relaxation times ( $T_1$  and  $T_2$ ) of aqueous solutions of SPIO-mPEG-8G7 nanoparticle complexes were measured to determine relaxivity,  $r_1$  and  $r_2$ . All measurements were made using a NMR relaxometer operating at 20 MHz and  $37.0 \pm 0.1$  °C (NMS-120 Minispec, Bruker). Before each measurement the relaxometer was tuned and calibrated. The values of  $r_1$  and  $r_2$  were determined from eight data points generated by inversion recovery and a Carr–Purcell–Meiboom–Gill pulse sequence, respectively.

### **2.2.4 *In vitro* MRI**

BxPC3 and PANC were cultured at 37 °C in humidified 5% CO<sub>2</sub> atmosphere. MRI was performed with a clinical 3.0-T magnetic resonance scanner (Sigma; GE Medical Systems, Milwaukee, WI, USA) and a knee coil. All cell lines contained  $2 \times 10^6$  cells and were incubated with SPIO-mPEG-8G7 nanoparticle (diluted in 1 mL medium, 0.3 mM Fe) for 30 min in an ice bath and then washed three times with PBS. All samples were scanned by a fast gradient echo pulse sequence (TR/TE/flip angle 3,000/90/10°.)

### **2.2.5 Synthesis of Graphene Nanosheet**

GNSs have been successively synthesized on GaN/Sapphire template, which was carried out in an ASTeXtype microwave plasma CVD system. In order to optimize the microwave discharge and the extension of the bias discharge over the entire substrate, we used a dome-shaped Mo anode which was placed above the substrate as counter-electrode. The ~3 μm thickness of GaN has been formed on sapphire substrate by metal-organic CVD. Prior to the deposition GNSs over it, the template was ultrasonically cleaned with acetone and alcohol for 12 min each. For carburization of template, we used 4 % CH<sub>4</sub> with 20 torr and microwave power was 550W. For the deposition of graphene over it, we used 2.9 % CH<sub>4</sub> with 40 torr and microwave power was 800W and bias voltage of - 100 V for 30 min and followed by further deposition for ~2 hr without bias the template. The GNSs was analyzed by a standard x-ray diffractometer (XRD) with a Cu K α source. The microstructure of theGNSs /GaN sample was evaluated with Raman microscopy (LABRAMHR)

## Chapter 3

# Results and Discussion

### 3.1 Physical Characteristics of SPIO-mPEG-8G7

The physical parameters of SPIO nanoparticle used for the study are shown in Table 4.

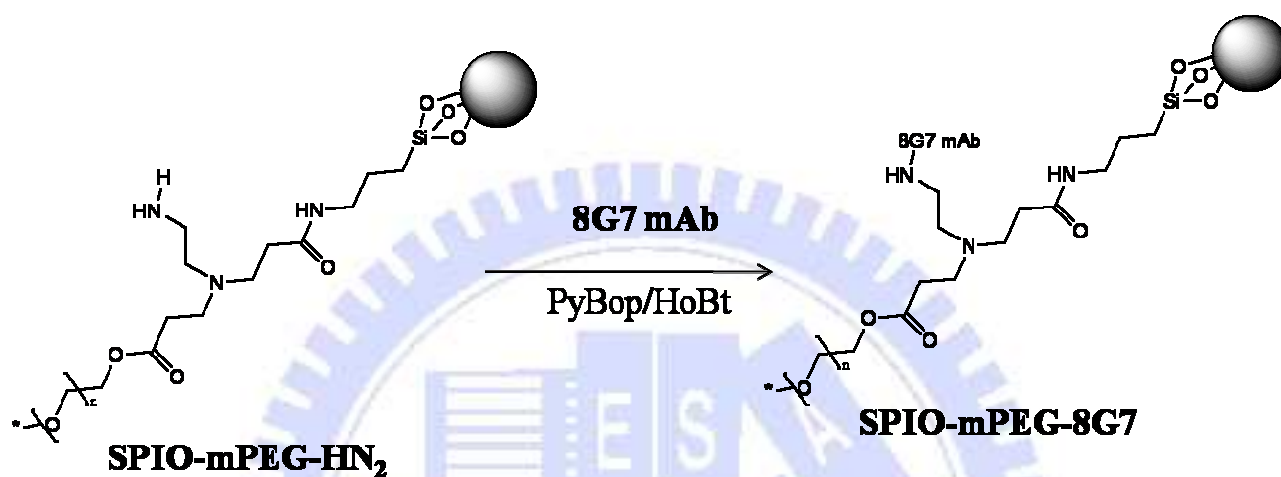
**Table 4** Physical properties of  $\text{MnFe}_2\text{O}_4$ <sup>a</sup>

Parameter	$\text{MnFe}_2\text{O}_4$
TEM (nm)	12.4 ± 0.9
<sup>b</sup> DLS(nm)	30.3 ± 5.7
<sup>b</sup> Relaxivity( $r_2/r_1$ )	238.4/36.9
Magnetization (emu/g)	84

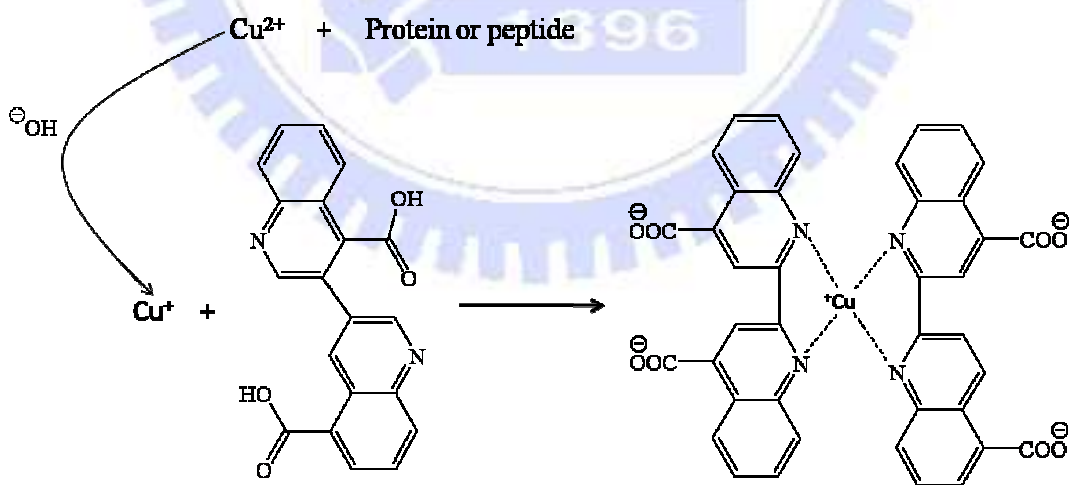
<sup>a</sup>Data obtained from Mr. John thesis. <sup>b</sup>The DLS and relaxivity data are based on SPIO-mPEG.

The  $-\text{NH}_2$  terminal of SPIO-mPEG-NH<sub>2</sub> has been used to conjugate 8G7 mAb on the surface of SPIO nanoparticle (Scheme 1). The Bicinchoninic Acid (BCA) protein assay was performed to confirm the presence of 8G7 mAb on the surface modification of SPIO-mPEG-NH<sub>2</sub>. Scheme 2 shows BCA-protein reaction mechanism. BCA serves the purpose of the Folin reagent in the Lowry assay, namely to react with complexes between copper ions and peptide bonds to produce a purple end product [90,91]. The change in color of BCA protein assay solution on adding SPIO-mPEG-8G7 from light blue to purple confirms the presence of 8G7 mAb on surface modification of SPIO. The hydrodynamic size distribution of SPIO-mPEG-NH<sub>2</sub> and SPIO-mPEG-anti-MUC4 was investigated by dynamic laser scattering (DLS) analysis system shown in Figure 10. The average diameter

for SPIO-mPEG-NH<sub>2</sub> and SPIO-mPEG-8G7 nanoparticle is 33.1 ± 2.3 nm and 45.4 ± 4.4 nm respectively.



**Scheme 1** Conjugation of 8G7 mAb on the surface of SPIO-mPEG-NH<sub>2</sub>, PyBop (benzotriazol-1-yloxy) tripyrrolidinophosphonium hexafluorophosphate, HoBt 1-hydroxybenzotriazole



**Scheme 2** BCA-Protein Reaction Mechanism



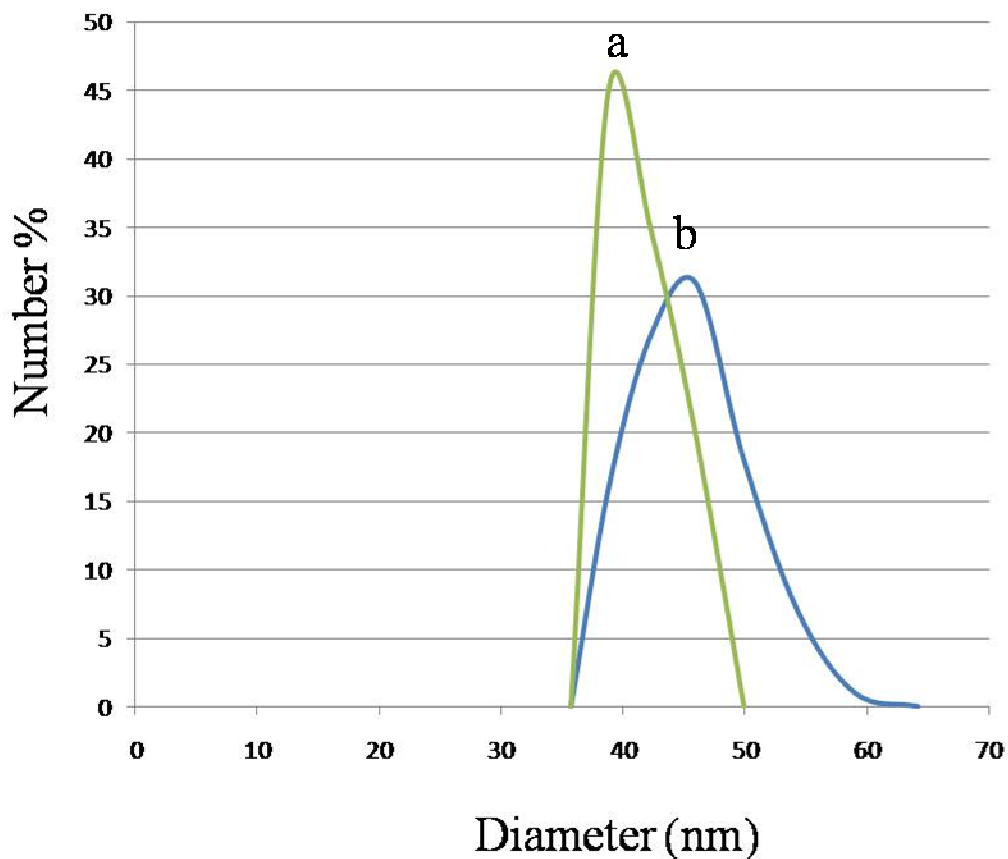


**Figure 10** Hydrodynamic diameters distribution (a) SPIO-mPEG-NH<sub>2</sub> (b) SPIO-mPEG-8G7

### 3.2 Relaxivity of SPIO-mPEG-8G7

In aqueous solution, the relaxivity values,  $r_1$  and  $r_2$ , of the SPIO-mPEG-8G7 at  $37.0 \pm 0.1$  °C and 20 MHz are 24.97 and 206.01  $\text{mM}^{-1} \text{s}^{-1}$ , respectively. The  $r_2$  value of SPIO-mPEG-8G7 is higher than that of clinically used Resovist ( $r_2 = 164 \text{ mM}^{-1} \text{ s}^{-1}$ ) [92]. The  $r_1$  value of SPIO-mPEG-8G7 and Resovist are similar ( $r_1 = 26 \text{ mM}^{-1} \text{ s}^{-1}$ ) [92].

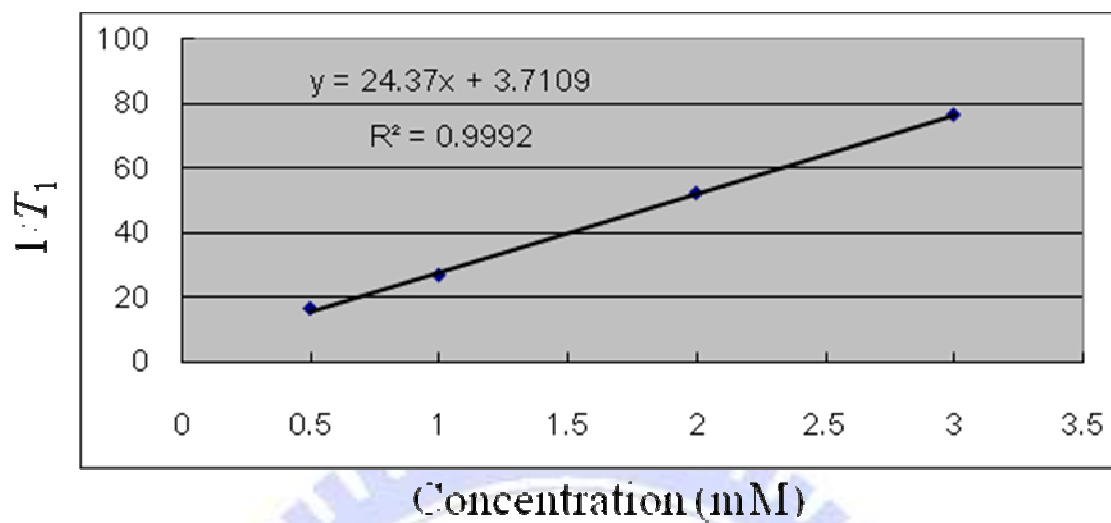


**Figure 11**  $T_1$  relaxation time of SPIO-mPEG-8G7

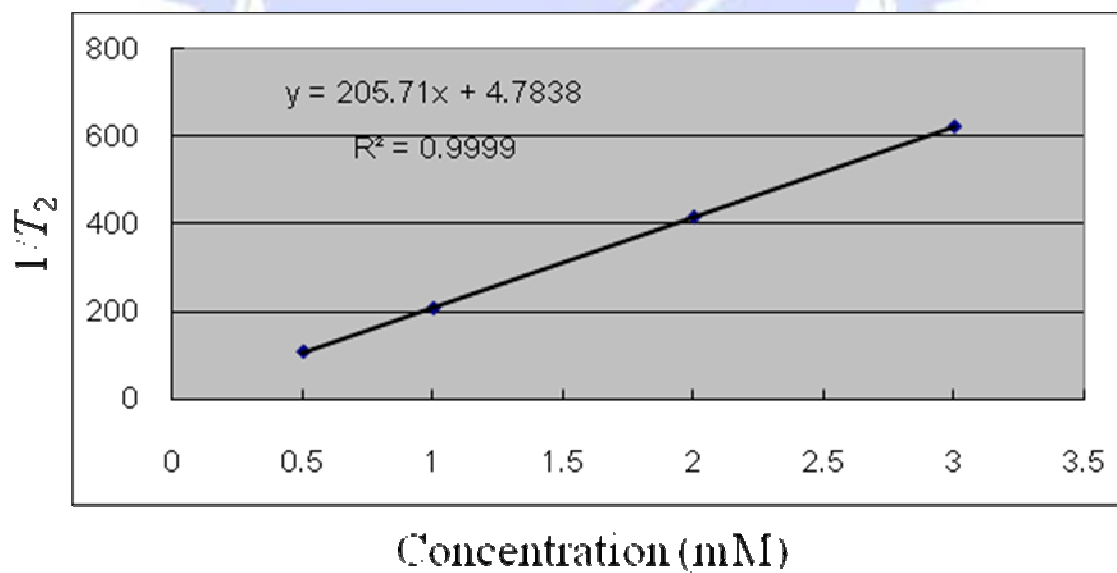


**Figure 12**  $T_2$  relaxation time of SPIO-mPEG-8G7

### 3.3 *In vitro* MRI

The targeting ability of SPIO-mPEG-8G7 nanoparticles was confirmed by *in vitro* MRI, as shown in Figure 13. BxPC3 which has a relatively high MUC4 expression level showed noticeable magnetic resonance contrast. However no contrast observed was observed in case of negatively express MUC4 mucine cell line, Panc1.

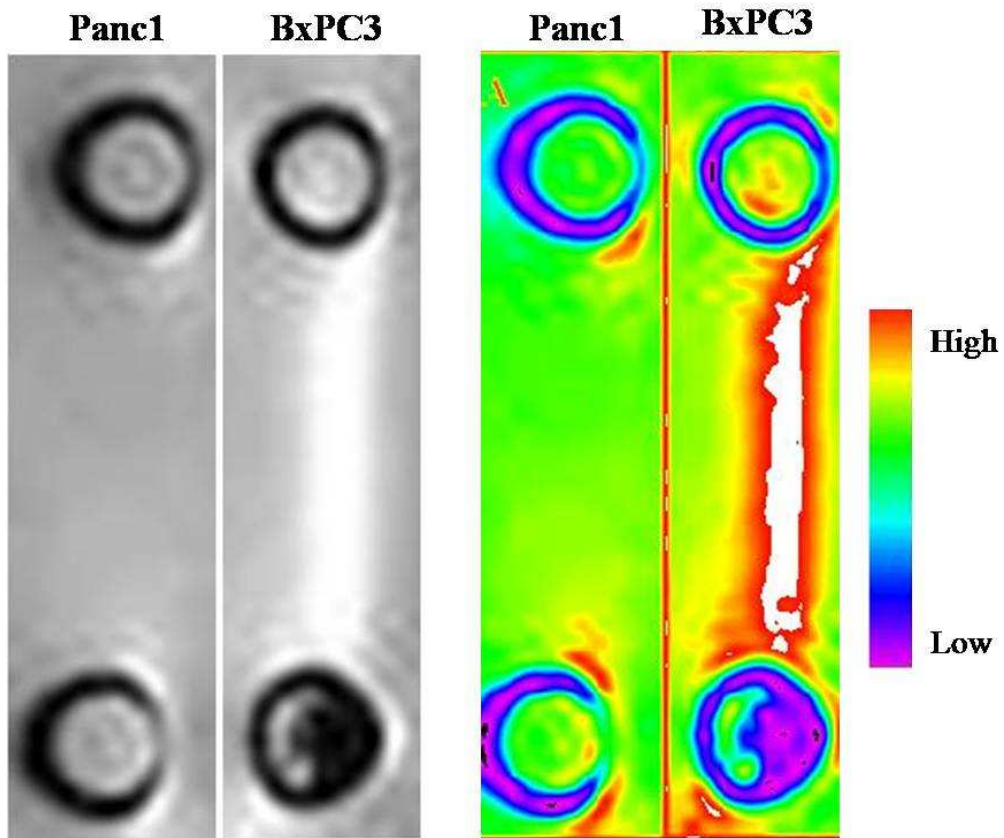


**Figure 13**  $T_2$ -weighted images of positive and negative cells for MUC4 expression after the treatment with or without 0.3 mM SPIO-mPEG-8G7 nanoparticles. The upper rows show cells without contrast agent treatment. The lower rows show cells treated with contrast agent. B color-map MRI

### 3.4 Structural Characterization of GNSs

The phase structure of the as-prepared final product was characterized by XRD. Figure 14 shows a typical XRD pattern of the as-prepared 3-D GNSs/spherical carbon/GaN. A sharp and intense XRD diffraction peak at about  $2\theta = 26.6^\circ$  can be indexed as the (002) diffraction, which reveals the high-quality graphitic nature of nanosheets. The weak and very sharp peaks at about  $2\theta = 34.8^\circ$  and  $2\theta = 45^\circ$  could be due to the GaN substrate and these two diffraction peaks are corresponding to (002) and (101) planes, respectively.

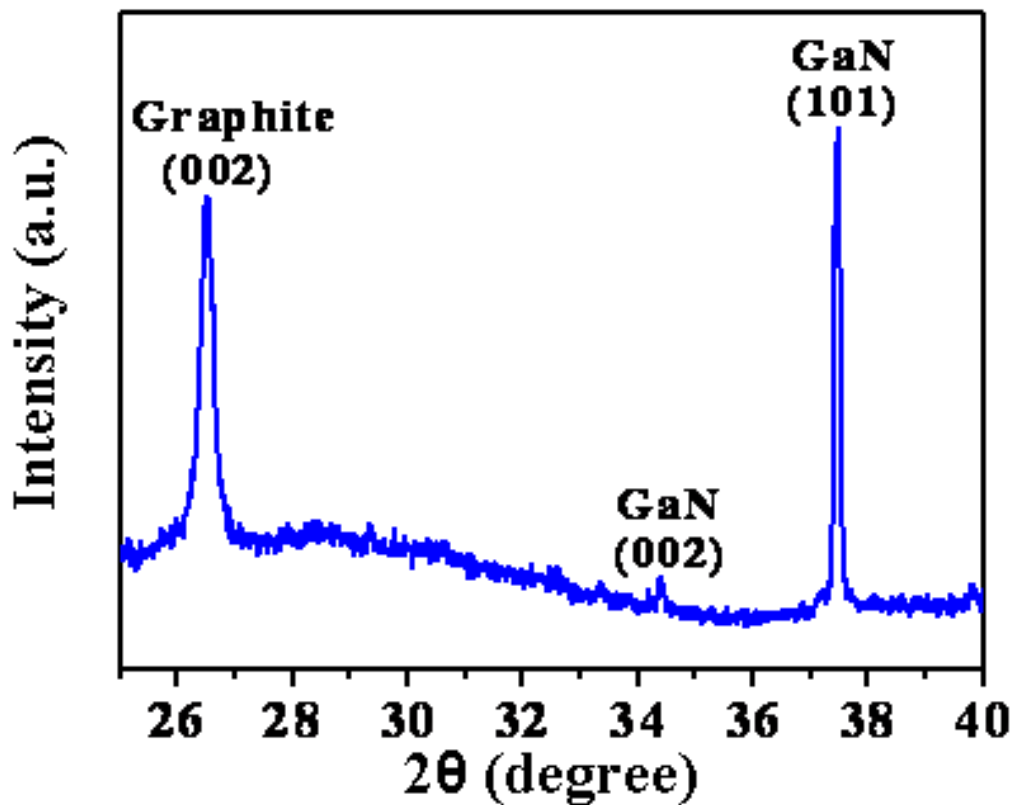


**Figure 14** XRD patterns of the GNSs/spherical carbon/GaN sample.

The thickness of the graphitic nanosheets along the (001) direction (i.e. the average crystallite size along the (001) direction) is about 56.6 nm estimated from the half-peak width of the (002) reflection peak using the Scherrer equation. This indicates that graphitization is complete and the degree of long-range order of these nanostructures is similar to that of bulk graphite [93]. The interlayer spacing is calculated to be  $\sim 0.34$  nm from the position of (002) reflection peak are similar to those observed for bulk hexagonal graphite ( $\sim 0.335$  nm) [93]. Later in, high-resolution transmission electron microscope (HRTEM) analysis was performed to confirm the interlayer spacing.

The morphologies of the 3-D GNSs/spherical carbon/GaN sample obtained under typical synthesis conditions were examined by using field-emission scanning electron microscopy (FESEM, JEOL JSM-6700F), transmission electron microscope (Philips TEM), selected-area electron diffraction (SAED), and HRTEM. Figure 15 (A-D) shows the typical FESEM images of the product prepared by microwave plasma CVD in presence of methane/hydrogen gas mixture.

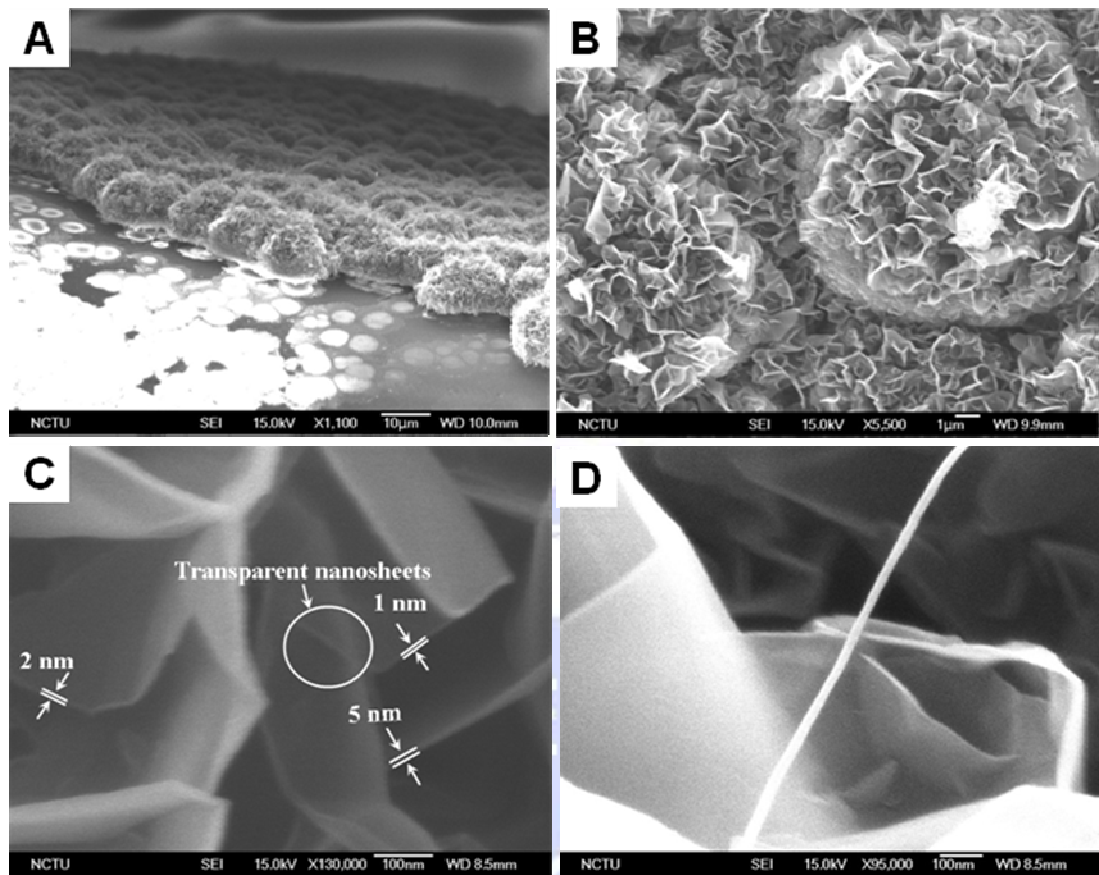


**Figure 15** (A) Side-view FESEM image of the GNSs/spherical carbons/GaN; (B-C) plane-view FESEM images of the GNSs/spherical carbons/GaN sample at different magnifications; (D) CNS.

Figure 15(A) and 14(B) show the low-resolution side view and plane view FESEM images of the 3-D GNS/spherical carbon/GaN sample. As shown in the FESEM image in Figure 15(A), the as-obtained 3-D GNS consists of spheres with diameters ranging from 9 to 10  $\mu\text{m}$ . The magnified FESEM images (Figure 15(B) shows that the surfaces of spheres are not smooth. And the microspheres look like completely covered by the 3-D GNSs. Figure 15(C) shows the high-resolution SEM image of the 3-D GNS/spherical carbon/GaN. According to Figure 15(C), transparent individual graphite clearly overlaps

on the other graphite structure. The higher magnification FESEM image (Figure 15C) clearly reveals that the GNSs have a thickness range 1 to 5 nm.

We have tried to nanoscrolls monolayer GNSs using isopropyl alcohol solution shown in Figure 15(D). Although preliminary result show formation of nanoscrolls from monolayer graphene however to confirm the result further investigation is in process. We believed that this can help us in drug loading.

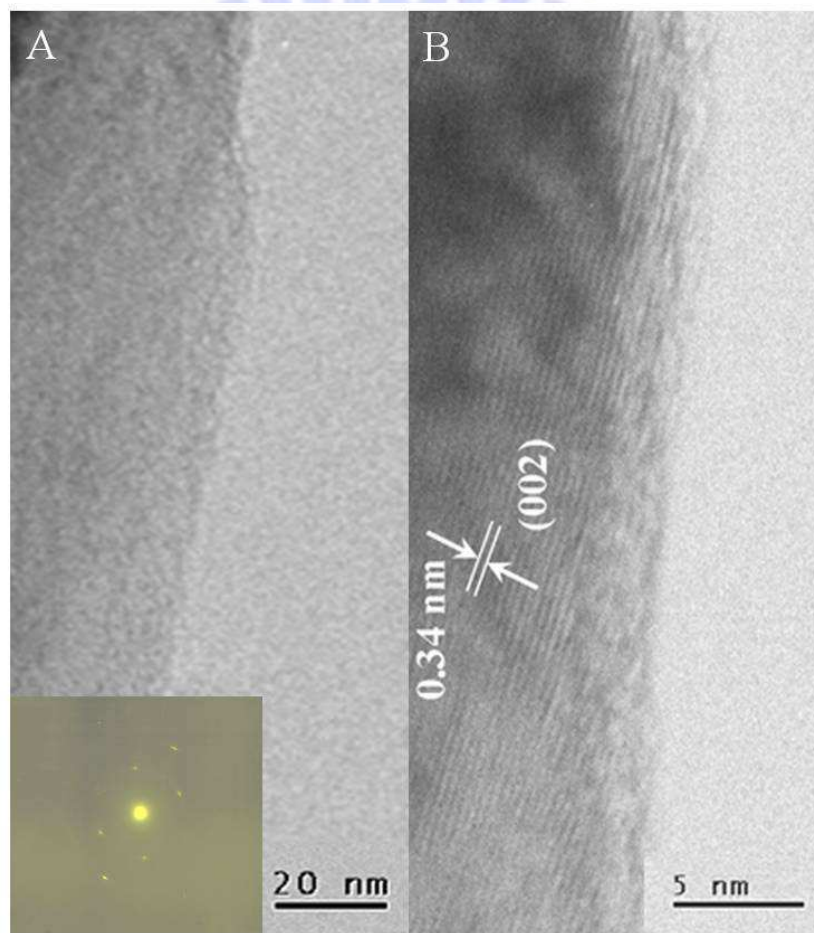


**Figure 16** TEM image of the individual GNS and the corresponding SAED pattern is shown in the inset, and (B) HRTEM of the individual GNS.

Figure 16(A) and 16(B) show the TEM image of an individual GNS and its corresponding SAED pattern with the electron beam directed along the individual GNS. The SAD pattern from the individual GNS shows few bright spots. The clearly visible bright spots confirm that the GNSs are single crystals. The HRTEM image taken at the top edge of the individual GNS shows that the interlayer distance about  $\sim 0.34$  nm, as shown in Figure 16(B). The lattice spacing of  $\sim 0.34$  nm corresponds to the (002) plane. This result is consistent with XRD data.

All the forms of carbon materials such as amorphous carbon, fullerenes, carbon nanotubes, polycrystalline carbon etc. have been characterized by Raman spectroscopy. The positions, half widths, and relative areas of spectral bands are governed by the nature of the chemical bonds of carbon. Therefore, the Raman spectrum may provide additional information about the as-prepared 3-D GNSs/spherical carbon/GaN structure. Raman spectra taken on GNSs, as shown in Figure 17, are similar to those observed for graphitic carbon [94]. Second order modes in the range of  $2000\text{--}3000\text{ cm}^{-1}$  are also present in Figure 17 shows that it has two strong peaks at  $1363$ , and  $1582\text{ cm}^{-1}$ . The peak at around  $1363\text{ cm}^{-1}$  is the D-band associated with vibrations of carbon atoms with dangling bonds in plane terminations of the disordered graphite. The peak at  $1576\text{ cm}^{-1}$  (G band) is attributed to the vibration of  $sp^2$ -bonded carbon atoms in a two-dimensional hexagonal lattice [95,96]. Figure 17 also shows that the strong peak at about  $2716\text{ cm}^{-1}$ , is attributed to the disorder mode 2D band.



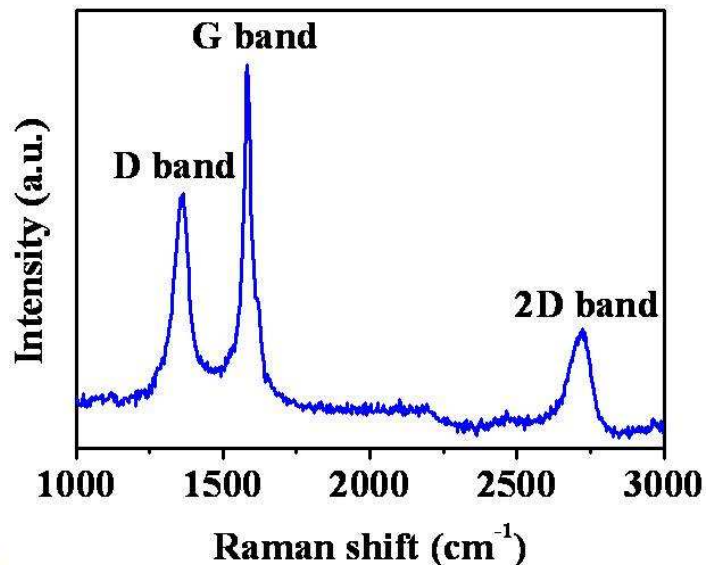


**Figure 17** Raman spectrums of the GNSs/spherical carbons/GaN sample.

From, Figure 17 we can see that, the G-band peak is stronger than the D-band peak and their intensity ratio is about 1.4 unambiguously suggests that the 3-D GNSs have high degree of graphitization. In addition, the area ratio between the two bands ( $A_D/A_G$ ) allows the degree of ordering or graphitization of the carbon structure to be characterized [97,98]. In the spectra of highly crystalline graphite, D-band is absent, which indicates the 100 %-degree of graphitization. It should be noted that the  $A_D/A_G$  value of GNSs (1.02) was smaller than that of Vulcan XC-72 and AP-carbon [99]. Furthermore, a similar value of  $A_D/A_G$  between GNSs (1.02) and MWCNT (1.03) [99] confirms that the 3-D GNSs retained similar graphitic characteristics to the MWCNT.

## **Conclusion**

The preliminary data of this study suggest SPIO-mPEG-8G7 nanoparticles are highly specific to MUC4 expression and it can be successfully used for early diagnosis of pancreatic cancer. This finding will be taken into account in highest priority for the development of carbon based  $T_2$  MRI contrast agent for early diagnosis of pancreatic cancer. As for now we have successfully synthesized GNSs in high yield.

## References

1. Parker, S. L.; Tong, T.; Bolden, S.; Wingo, P. A. *CA Cancer J Clin.* **1997**, *47*, 5.
2. Yang, C. Y.; Chiu, H. F.; Cheng, M. F.; Tsai, S. S.; Hung, C. F.; Tseng, Y. T. *J Toxicol Environ Health A* **1999**, *56*, 361.
3. Sing, A. P.; Moniaux, N.; Chauhan, S. C.; Meza, J. L.; Batra, S. K. *Cancer Res.* **2004**, *64*, 622.
4. Fernandez, E.; La Vecchia, C.; Porta, M.; Negri, E.; Lucchini, F.; Levi, F. *Int. J. Cancer* **1994**, *57*, 786.
5. Kuwahara, K.; Sasaki, T.; Kuwada, Y.; Murakami, M.; Yamasaki, S.; Chayama, K. *Pancreas* **2003**, *26*, 344.
6. Duffy, M. J.; Sturgeon, C.; Lamerz, R.; Haglund, C.; Holubec, V. L.; Klapdor, R.; Nicolini, A.; Topolcan, O.; Heinemann, V. *Ann Oncol.* **2009**, doi:10.1093/annonc/mdp332
7. Locker, G. Y.; Hamilton, S.; Harris, J.; Jessup, J. M.; Kemeny, N.; Macdonald, J. S.; Somerfield, M. R.; Hayes, D. F.; Bast, R. C. Jr. *J Clin Oncol.* **2006**, *24*, 5313.
8. Warshaw, A. L.; Fernandez-del, C. C. *N. Engl. J. Med.* **1992**, *326*, 455.
9. Price-Schiavi, S. A.; Perez, A. B., R.; Carraway, K. L. *Biochem J.* **2000**, *349*, 641.
10. Moniaux, N.; Andrianifahanana, M.; Brand, R. E.; Batra, S. K. *Br J Cancer* **2004**, *91*, 1633.
11. Swartz, M. J.; Batra, S. K.; Varshney, G. C. *Am J Clin Pathol.* **2002**, *117*, 791.
12. Singh, A. P.; Chaturvedi, P.; Batra, S. K. *Cancer Res.* **2007**, *67*, 433.
13. Bloch, F. *Phys. Rev.* **1946**, *70*, 460.
14. Bloch, F.; Hansen, W. W.; Packard, M. *Phys. Rev.* **1946**, *70*, 474.

15. Purcell, E. M.; Torrey, H. C.; Pound, R. V. *Phys. Rev.* **1946**, *69*, 37.
16. (a) Polášek, M.; Šedinová, M.; Kotek, J.; Vander Elst, L.; Muller, R. N.; Hermann, P.; Lukeš, I. *Inorg. Chem.* **2009**, *48*, 455. (b) Frangioni, J. V. *Nat. Biotechnol.* **2006**, *24*, 909.
17. De, M.; Chosh, P. S.; Rotello, V. M. *Adv. Mater.* **2008**, *20*, 4225.
18. Cai, W.; Hsu, A. R.; Li, Z. B.; Chen, X. *Nanoscale Res. Lett.* **2007**, *2*, 265.
19. Lacerda, L.; Bianco, A.; Prato, M.; Kostarelos, K. *Adv. Drug Deliv. Rev.* **2006**, *58*, 1460.
20. Hirsch, L. R.; Gobin, A. M.; Lowery, A. R.; Tam, F.; Drezek, R. A.; Halas, N. J. *Ann. Biomed. Eng.* **2006**, *34*, 15.
21. Thorek, D. L.; Chen, A. K.; Czupryna, J.; Tsourkas, A. *Ann. Biomed. Eng.* **2006**, *34*, 23.
22. Emerich, D. F.; Thanos, C. G. *Biomol Eng.* **2006**, *23*, 171.
23. Gossuin, Y.; Gillis, P.; Hocq, A.; Vuong, Q. L.; Roch, A. *WIREs Nanomed Nanobiotechnol* **2009**, *1*, 299.
24. Seo, W. S.; Lee, J. H.; Sun, X.; Suzuki, Y.; Mann, D.; Liu, Z.; Terashima, M.; Yang, P. C.; McConnell, M. V.; Nishimura, D. G.; Dai, H. *Nat. Mater.* **2006**, *5*, 971.
25. Chavanpatil, M. D.; Khdair, A.; Panyam, J.; *J. Nanosci. Nanotechnol.* **2006**, *6*, 2651.
26. Shamsi, K.; Balzer, T.; Saini, S.; Ros, P. R.; Nelson, R. C.; Carter, E. C.; Tollerfield, S.; Niendorf, H. P. *Radiology* **1998**, *206*, 365.
27. Weissleder, R.; Stark, D. D.; Rummeny, E. J.; Compton, C. C.; Ferrucci, J. T. *Radiology* **1988**, *166*, 423.

28. Mack, M. G.; Balzer, J. O.; Straub, R.; Eichler, K.; Vogl, T. J. *Radiology* **2002**, 222, 239.
29. Sun, C.; Lee, J. S. H.; Zhang, M. *Adv Drug Deliv Rev.* **2008**, 60, 1252.
30. Bachilo, S. M.; Strano, M. S.; Kittrell, C.; Hauge, R. H.; Smalley, R. E.; Weisman, R. B. *Science* **2002**, 298, 2361.
31. Hartschuh, A.; Pedrosa, H. N.; Novotny, L.; Krauss, T. D. *Science* **2003**, 301, 1354.
32. O'Connell, M. J.; Bachilo, S. M.; Huffman, C. B.; Moore, V. C.; Strano, M. S.; Haroz, E. H.; Rialon, K. L.; Boul, P. J.; Noon, W. H.; Kittrell, C.; Ma, J.; Hauge, R. H.; Weisman, R. B.; Smalley, R. E. *Science* **2002**, 297, 593.
33. Moon, H. K.; Lee, S. H.; Choi, H. C. *ACS Nano* **2009**, doi: 10.1021/nn900904h
34. Choi, J. H.; Nguyen, F. T.; Barone, P. W.; Heller, D. A.; Moll, A. E.; Patel, D.; Boppart, S. A.; Strano, M. S. *Nano Lett.* **2007**, 7, 861.
35. Coskun, U. C.; Wei, T. C.; Vishveshwara, S.; Goldbart, P. M.; Bezryadin, A. *Science* **2004**, 304, 1132.
36. Singh, A. P.; Chauhan, S. C.; Bafna, S.; Johansson, S. L.; Smith, L. M.; Moniaux, N.; Lin, M. F.; Batra, S. K. *Prostate* **2006**, 66, 421.
37. Bafna, S.; Singh, A. P.; Moniaux, N.; Eudy, J. D.; Meza, J. L.; Batra, S. K. *Cancer Res.* **2008**, 68, 9231.
38. Moniaux, N.; Varshney, G. C.; Chauhan, S. C.; Copin, M. C.; Jain, M.; Wittel, U. A.; Andrianifahanana, M.; Aubert, J. P.; Batra, S. K. *J Histochem Cytochem.* **2004**, 52, 253.

39. Moniaux, N.; Chaturvedi, P.; Van Seuning, I.; Porchet, N.; Singh, A.P.; Batra, S.K. Atlas Genet Cytogenet Oncol Haematol. February 2007. URL : <http://AtlasGeneticsOncology.org/Genes/MUC4ID41459ch3q29.html>
40. Andrianifahanana, M.; Moniaux, N.; Schmied, B. M.; Ringel, J.; Friess, H.; Hollingsworth, M. A.; Buchler, M. W.; Aubert, J. P.; Batra, S. K. *Clin Cancer Res.* **2001**, 7, 4033.
41. Chaturvedi, P.; Singh, A. P.; Batra, S. K. *FASEB J.* **2008**, 22, 966.
42. Nollet, S.; Moniaux, N.; Maury, J.; Petitprez, D.; Degand, P.; Laine, A.; Porchet, N.; Aubert, J. P. *Biochem J.* **1998**, 332, 739.
43. McRobbie, D. W. M., E. A.; Graves, M. J.; Prince, M. R. *MRI from Picture to Proton, Second Edition, Cambridge University Press*
44. Wendland, M. F. *NMR Biomed.* **2004**, 17, 581.
45. Caravan, P.; Ellison, J. J.; McMurry, T. J.; Lauffer, R. B. *Chem.Rev.* **1999**, 99, 2293.
46. Aime, S.; Fasano, M.; Terreno, E.; Botta, M. *The Chemistry of Contrast Agents in Medical Magnetic Resonance Imaging; John Wiley and Sons: New York.* **2001**.
47. Lawaczeck, R.; Menzel, M. P., H. *Appl. Organomet. Chem.* **2004**, 18, 506.
48. Willard, M. A.; Kurihara, L. K.; Carpenter, E. E.; Calvin, S.; Harris, V. G. *Int. Mater. Rev.* **2004**, 49, 125.
49. Geraldes, C.F.; Laurent, S. *Contrast Media Mol Imaging* **2009**, 4, 1.
50. Aime, S.; Crich, S. G.; Gianolio, E.; Giovenzana, G. B.; Tei, L.; Terreno, E. *Coord. Chem. Rev.* **2006**, 250, 1562.
51. Khemtong, C.; Kessinger, C. W.; Gao, J. *Chem. Commun.* **2009**, 3497.

52. Skomski, R.; Coey, J. M. D. *Permanent Magnetism, Institute of Physics Publishing, Bristol and Philadelphia, 1999.*
53. Leslie-Pelecky, D. L.; Rieke, R. D. *Chem. Mater* **1996**, 8, 1770.
54. Neel, L. C. R. *Acad. Sci.* **1949**, 228, 664.
55. Barbara, B. *Magnetism and Synchrotron Radiation, Springer Berlin / Heidelberg, 2001.*
56. Bjørnerud, A.; Johansson, L. *NMR Biomed.* **2004**, 17, 465.
57. Chin, A. B.; Yaacob, I. I. *J. Mater. Process. Technol.* **2007**, 191, 235.
58. Albornoz, C.; Jacobo, S. E. *J. Magn. Magn. Mater.* **2006**, 305, 12.
59. Kim, E. H.; Lee, H. S.; Kwak, B. K.; Kim, B. K. *J. Magn. Magn. Mater.* **2005**, 289, 328.
60. Wan, J.; Chen, X.; Wang, Z.; Yang, X.; Qian, Y. *J. Cryst. Growth* **2005**, 276, 571.
61. Kimata, M.; Nakagawa, D.; Hasegawa, M. *Powder Technol.* **2003**, 132, 112.
62. Alvarez, G. S.; Muhammed, M.; Zagorodni, A. A. *Chem. Eng. Sci.* **2006**, 61, 4625.
63. Basak, S.; Chen, D.-R.; Biswas, P. *Chem. Eng. Sci.* **2007**, 62, 1263.
64. Cornell, R. M.; Schwertmann, U. *The Iron Oxides*; VCH Publishers: Weinheim, Germany, **1996**.
65. Boistelle, R.; Astier, J. P. *J. Cryst. Growth* **1988**, 90, 14.
66. Sugimoto, T. *Chem. Eng. Technol.* **2003**, 26, 3.
67. Gupta, A. K.; Gupta, M. *Biomaterials* **2005**, 26, 3995.
68. Sun, S.; Zeng, H.; Robinson, D. B.; Raoux, S.; Rice, P. M.; Wang, S. X.; Li, G. *J. Am. Chem. Soc.* **2004**, 126, 273.
69. Xu, C.J.; Sun, S.H. *Polymer Int.* **2007**, 56, 821.

70. Lee, J.H.; Huh, Y.M.; Jun, Y.W.; Seo, J.W.; Jang, J.-T.; Song, H.T.; Kim, S.; Cho, E.J.; Yoon, H.G.; Suh, J.S.; Cheon, J. *Nat. Med.* **2007**, *13*, 95.
71. Lee, H.; Lee, E.; Jeong, Y. Y.; Kim, D. K.; Jang, N. K.; Jon, S. *J. Am. Chem. Soc.* **2006**, *128*, 7383.
72. Iijima, S. *Nature* **1991**, *354*, 56.
73. Kocabas, C.; Kang, S. J.; Ozel, T.; Shim, M.; Rogers, J. A. *J. Phys. Chem. C* **2007**, *111*, 17879.
74. Ajayan, P. M. *Chem. Rev.* **1999**, *99*, 1787.
75. Gannon, C. J.; Cherukuri, P.; Yakobson, B. I.; Cagnet, L.; Kanzius, J. S.; Kittrell, C.; Weisman, R. B.; Pasquali, M.; Schmidt, H. K.; Smalley, R. E.; Curley, S. A. *Cancer* **2007**, *110*, 2654.
76. Zavaleta, C.; de la Zerda, A.; Liu, Z.; Keren, S.; Cheng, Z.; Schipper, M.; Chen, X.; Dai, H.; Gambhir, S. S. *Nano Lett.* **2008**, *8*, 2800.
77. Zhang, Y.; Tan, J. W.; Stormer, H. L.; Kim, P. *Nature* **2005**, *438*, 201.
78. Han, M. Y.; Oezylmaz, B.; Zhang, Y.; Kim, P. *Phys. Rev. Lett.* **2007**, *98*, 206805.
79. Bolotin, K. I.; Sikes, K. J.; Jiang, Z.; Klima, M.; Fudenberg, G.; Hone, J.; Kim, P.; Stormer, H. L. *Solid State Commun* **2008**, *146*, 351.
80. Lee, C.; Wei, X.; Kysar, J. W.; Hone, J. *Science* **2008**, *321*, 385.
81. Bunch, J. S.; van der Zande, A. M.; Verbridge, S. S.; Frank, I. W.; Tanenbaum, D. M.; Parpia, J. M.; Craighead, H. G.; McEuen, P. L. *Science* **2008**, *315*, 490.
82. Singh, R.; Kroll, P. *J. Phys.: Condens. Matter* **2009**, *21*, 196002.
83. Takahashi, M.; Turek, P.; Nakazawa, Y.; Tamura, M.; Nozawa, K.; Shiomi, D.; Ishikawa, M.; Kinoshita, M. *Phys. Rev. Lett.* **1991**, *67*, 746.



84. Novoselov, K. S.; Geim, A. K.; Morozov, S. V.; Jiang, D.; Zhang, Y.; Dubonos, S. V.; Grigorieva, I. V.; Firsov, A. A. *Science* **2004**, *306*, 666.
85. Xie, X.; Ju, L.; Feng, X.; Sun, Y.; Zhou, R.; Liu, K.; Fan, S.; Li, Q.; Jiang, K. *Nano Lett.* **2009**, *9*, 2565.
86. Yu, D.; Liu, F. *Nano Lett.* **2007**, *7*, 3046.
87. Richard, C.; Doan, B. T.; Beloeil, J. C.; Bessodes, M.; Tóth, E.; Scherman, D. *Nano Lett.* **2008**, *8*, 232.
88. Ananta, J. S.; Matson, M. L.; Tang, A. M.; Mandal, T.; Lin, S.; Wong, K.; Wong, S. T.; Wilson, L. J. *J. Phys. Chem. C* **2009** doi: 10.1021/jp907891n.
89. Wang, S.; Tang, L. A. I.; Bao, Q.; Lin, M.; Deng, S.; Goh, B. M.; Loh, K. P. *J. Am. Chem. Soc.* **2009**, doi: 10.1021/ja905968v.
90. Smith, P. K. *Anal. Biochem.* **1985**, *150*, 76.
91. Tylianakis, P. E. *Anal. Biochem.* **1994**, *219*, 335.
92. Horák, D.; Babič, M.; Jendelová, P.; Herynek, V.; Trchova, M.; Pientka, Z.; Pollert, E.; Hájek, M.; Syková, E. *Bioconjug Chem.* **2007**, *8*, 635.
93. Zhang, H.B.; Lin, G.D.; Zhou, Z.H.; Dong, X.; Chen, T. *Carbon* **2002**, *40*, 2429.
94. Reich S.; Thomsen, C. *Phil. Trans. R. Soc. Lond. A* **2004**, *362*, 2271.
95. Liu, J. W.; Shao, M. W.; Chen, X. Y.; Yu, W. C.; Liu, X. M.; Qian, Y. T. *J. Am. Chem. Soc.* **2003**, *125*, 8088.
96. Liu, J. W.; Shao, M. W.; Tang, Q.; Zhang, S. Y.; Qian, Y. T. *J. Phys. Chem. B* **2003**, *107*, 6329.
97. Kim, P.; Joo, J. B.; Kim, W.; Kim, J.; Song, I.K.; Yi, J. *Catal. Lett.* **2006**, *112*, 213.

98. Maldonado, F.; Moreno, C.; Rivera, J.; Hanzawa, Y.; Yamada, Y. *Langmuir* **2000**, *16*, 4367.

99. Joo, J. B.; Kim, Y. J.; Kim, W.; Kim, P.; Yi, J. *Catalysis Commun.* **2008**, *10*, 267.

